

Transport of aerosols into the UTLS and their impact on the Asian monsoon region as seen in a global model simulation

Suvarna Fadnavis¹, Kirill Semeniuk², Luca Pozzoli³, Martin G. Schultz⁴, Sachin D. Ghude¹, Subrata Das¹, Rashmi Kakatkar¹

¹Indian Institute of Tropical Meteorology, Pune India.

²Department of Earth and Space Sciences and Engineering, York University, Toronto, Canada.

³Eurasia Institute of Earth Sciences, Istanbul Technical University, Turkey.

⁴Institute for Energy and Climate Research-Troposphere (IEK-8), Forschungszentrum, Jülich, Jülich, Germany.

Abstract:

An eight member ensemble of ECHAM5-HAMMOZ simulations for a typical boreal summer season is analyzed to study the transport of aerosols in the Upper Troposphere and Lower Stratosphere (UTLS) during the Asian Summer Monsoon (ASM). The simulations show persistent maxima in black carbon, organic carbon, sulfate, and mineral dust aerosols within the anticyclone in the UTLS throughout the ASM (period from July to September) when convective activity over the Indian subcontinent is highest, indicating that boundary layer aerosol pollution is the source of this UTLS aerosol layer. The simulations identify deep convection and the associated heat driven circulation over the southern flanks of the Himalayas as the dominant transport pathway of aerosols and water vapour into the tropical tropopause layer (TTL). Comparison of model simulations with and without aerosols indicates that anthropogenic aerosols are central to the formation of this transport pathway. Aerosols act to increase cloud ice, water vapour and temperature in the model UTLS. Evidence of ASM transport of aerosols into the stratosphere is also found, in agreement with aerosol extinction measurements from the HALogen Occultation Experiment (HALOE) and Stratospheric Aerosol and Gas Experiment (SAGE) II. As suggested by the observations, aerosols are transported into the southern hemisphere around the tropical tropopause by large scale mixing processes. Aerosol induced

circulation changes also include a weakening of the main branch of the Hadley circulation and a reduction of monsoon precipitation over India.

Key words: Aerosol pollution; Convective transport; Upper troposphere and lower stratosphere; ECHAM5-HAMMOZ model; Asian summer monsoon.

1. Introduction

East Asia is one of the largest source region of gaseous and aerosol pollutants, having both high anthropogenic emissions and important natural sources such as wildfires and dust storms (Park et al., 2010; Jeong et al., 2011). Developing nations of East Asia are experiencing [dramatic increase in the levels](#) of aerosol pollution, because of the rapid industrialization (Liu & Diamond, 2005; Venkataraman et al., 2005). The increase in atmospheric concentrations of [anthropogenic aerosols](#) (including black carbon, organic carbon, and sulfate) from such sources as transportation, industry, agriculture, and urban land development affect weather and climate (IPCC, 2007). Absorbing aerosols such as dust and black carbon heat the atmosphere due to shortwave absorption. Non-absorbing aerosols such as sulfate cause surface cooling by scattering solar radiation, [and](#) have a relatively small heating effect on the atmosphere itself. Both absorbing and non-absorbing aerosols cause a solar dimming effect by blocking part of the solar radiation from reaching the earth surface ([Wild, 2009](#); Ramanathan et al., 2005; Lau et al., 2006). Recent studies suggest that increased aerosol loading may change the energy balance in the atmosphere and at the Earth's surface, and alter the global water cycle (IPCC, 2007) [with important consequences for the Indian summer monsoon](#). Ramanathan et al. (2005) reported that the polluted layer of black carbon, organic carbon and dust over the Asian monsoon region leads to a weakening of the summer monsoon rainfall [based on ensemble simulations](#). However, Lau et al. (2006) argued that absorbing aerosols over the elevated Tibetan plateau with its high surface albedo should intensify the Indian summer monsoon through the increased heat pump effect.

Numerical experiments have suggested that atmospheric circulation anomalies induced by black carbon may be a cause of drought over Northern China and of excessive rain fall over Southern China and India (Menon et al., 2002). These studies indicate that aerosol effects can

induce large changes in precipitation patterns, which in turn may [change climate on a regional or even global scale](#).

Aerosol-induced circulation changes might furthermore affect the vertical transport of [pollution from the surface into the UTLS](#). Recent satellite observations [provide evidence](#) that the ASM circulation provides a pathway for pollution transport into the stratosphere (Randel et al., 2010) [with potential implication for stratosphere dynamics](#). A persistent maximum of tropospheric chemical constituents (H_2O , CO , C_2H_6 , CH_4 , N_2O , HCN , and aerosols) have been observed inside the ASM anticyclone in the UTLS during boreal summer (Park et al., 2004; Li et al., 2005; Randel and Park 2006; Fu et al., 2006; Xiong et al., 2009; Randel et al., 2010). [These results have been confirmed by modeling studies \(Park et al., 2007, Chen et al., 2012; Randel et al., 2010; Li et al., 2005\)](#). Recently, a layer of aerosols at the tropopause during the Asian monsoon has been observed in CALIPSO lidar measurements (Vernier et al., 2011). The UTLS aerosol layer extends from the Eastern Mediterranean to Western China and vertically from 13 to 18km, [indicating role of deep convection associated with the monsoon in transporting aerosols in the upper troposphere](#).

Observations and modeling studies suggest that the occurrence of aerosol layers near the tropopause could strongly affect [the formation of cirrus](#) clouds and precipitation (Li et al., 2005; Yin et al., 2005; Su et al., 2011). The influence of anthropogenic aerosols (sulfate and soot) on upper tropospheric (UT) clouds through ice nucleation was studied by Liu et al. (2009) using the NCAR Community Atmospheric Model Version 3 (CAM3). They reported that the homogeneous freezing of sulfate particles dominates cirrus cloud formation in the upper troposphere. Anthropogenic sulfate results in a global annual mean change of long-wave cloud forcing (LWCF) of $0.20 \pm 0.09 \text{ W m}^{-2}$ and short-wave cloud forcing (SWCF) of $0.30 \pm 0.17 \text{ W m}^{-2}$.

² and an increase of UTLS water vapor by ~10%. When both homogeneous and heterogeneous ice nucleation [are taken into account](#), anthropogenic soot may increase global cirrus cloud cover by ~2% and UTLS water vapor by 40% with a change in LWCF of 1.5 W m^{-2} . Su et al. (2011) hypothesized that aerosol semi-direct radiative heating and changes in cirrus radiative heating may contribute to the observed increase in tropical tropopause layer temperatures and to elevated water vapour concentrations in polluted clouds. Several other studies (e.g. Randall et al., 1989; Ramaswamy and Ramanathan, 1989; Liu et al., 2003a,b; Dodion et al., 2008) pointed out that cirrus clouds are likely to affect the intensity of the large-scale circulation in the tropics.

In the stratosphere aerosols have much longer residence time than in the troposphere and they get dispersed over a larger area. Through their interaction with ultraviolet, visible and infrared radiation, stratospheric aerosols are likely to play a significant role in the Earth's radiation budget and climate (Dodion et al., 2008). Simulations of stratospheric geo-engineering with sulphate (Heckendorn et al., 2009) or black carbon (BC) aerosols (Kravitz et al., 2012) show that continuous injection of aerosol into the lower stratosphere would cause large changes in UTLS temperatures.

[As can be seen from the above discussions the ASM plays a dominant role in the transport of boundary layer pollution into the UTLS.](#) Fu et al. (2006) argued based on observational evidence that the region poleward of 25°N encompassing the southern slopes of the Himalayas and the Tibetan plateau provides the main pathway for cross-tropopause transport. While Park et al (2009) concluded based on CTM simulations that deep monsoon convection south of 25°N over the Bay of Bengal and extending to the South China Sea is the primary entry point into the UTLS. According to the Park et al. analysis, convection in this region transports boundary layer pollutants up to ~200 hPa and a fraction of the air is advected by large scale upward motion on

the eastern side of the anticyclone to 16 km and becomes trapped within it. These differing pictures of the transport pathways indicate that there is need for additional research to increase our understanding. The purpose of the study presented here is to use a GCM with fully coupled aerosol effects on convection and radiative transfer to investigate the impact of aerosols on transport in the ASM region. Aerosols affect the energy balance and alter the hydrological cycle, so they have the potential to significantly impact the circulation and transport over the ASM region.

We employ the state-of-the-art ECHAM5-HAMMOZ aerosol-chemistry-climate model (Pozzoli et al., 2008a, 2011) to simulate black carbon (BC), organic carbon (OC), mineral dust and sulfate (SO_4^{2-}) aerosols during a typical Asian summer season. The model results are evaluated through comparison with HALOE and SAGE II data. To understand the effect of aerosols, the difference between model simulations with fully interactive aerosols (CTRL) and with only passively transported aerosol (NOAER) are analyzed. The paper is organized as follows. The ECHAM5-HAMMOZ model and satellite data (SAGE II and HALOE) are described in section 2. The influence of ASM convection on the distribution of aerosols in the UTLS is discussed in section 3 and impact of aerosols on cloud ice, temperature, water vapor and changes in circulation and precipitation are presented in section 4. Section 5 concludes this study.

2. Model simulations and data analysis

2.1 ECHAM5-HAMMOZ Model simulation and experimental setup

The ECHAM5-HAMMOZ aerosol-chemistry-climate model used in the present study comprises the general circulation model ECHAM5 (Roeckner et al., 2003), the tropospheric chemistry module, MOZ (Horowitz et al., 2003), and the aerosol module, Hamburg Aerosol Model (HAM) (Stier et al., 2005). The tropospheric chemistry module MOZ and the aerosol module HAM are fully interactive and implemented together in ECHAM5 (Pozzoli et al., 2008a). The HAM module takes into account the major aerosol compounds namely sulfate, black carbon, organic carbon, sea salt and mineral dust. It represents aerosols as internal and external mixtures with four soluble and three insoluble modes (Vignati et al., 2004). Details of the aerosol categorization and their parameterization schemes are documented by Stier et al. (2005). The chemical scheme used in the tropospheric chemistry module, MOZ is identical to the MOZART-2 model with small modifications as described by Pozzoli et al. (2008a). It includes 63 tracers and 168 reactions to represent O_x - NO_x -hydrocarbon chemistry.

We used the RETRO project data set of the year 2000 (<http://www.retro.enes.org/>) for the surface CO , NO_x , and hydrocarbon emissions from anthropogenic sources and biomass burning (Schultz et al., 2008). The anthropogenic and fire emissions of SO_2 , BC and OC are based on the AEROCOM emission inventory (Dentener et al., 2006) representative of the year 2000. The anthropogenic and natural emissions are also described in detail by Pozzoli et al. (2008a,b).

The emissions from vegetation of CO and VOCs (isoprene and terpenes) were calculated interactively using the Model of Emissions of Gases and Aerosols from Nature (MEGAN) (Guenther et al., 2006). Lightning NO_x emissions are calculated following the parameterization of Grewe et al. (2001). DMS, predominantly emitted from the oceans, is an SO_2 -4 aerosol

precursor. Its emissions depend on seawater DMS concentrations associated with phytoplankton blooms (Kettle and Andreae, 2000) and model surface wind speed, which determines the DMS sea-air exchange (Nightingale et al., 2000). Terrestrial biogenic DMS emissions follow Pham et al. (1995). The emissions of sea salt are based on Schulz et al. (2004). Mineral dust emissions are calculated online using the ECHAM5 wind speed, hydrological parameters (e.g. soil moisture), and soil properties, following the work of Tegen et al. (2002) and Cheng et al. (2008).

Stratospheric NO_x , HNO_3 , and CO concentrations are supplied as 3-D monthly means from simulations of the MOZART-3 model (Kinnison et al., 2007). Stratospheric O_3 concentrations are prescribed as monthly mean zonal climatology derived from observations (Randel et al., 1998; Logan, 1999). These concentrations are fixed at the topmost two model levels (pressures of 30 hPa and above). At other model levels above the tropopause, the concentrations are relaxed toward the climatological values with a relaxation time of 10 days following Horowitz et al. (2003). The tropopause height is diagnosed as the lowest level at which the lapse rate decreases to 2°C per kilometer or less following the World Meteorological Organization definition (WMO, 1992).

The ECHAM5, HAM and MOZ model performance against observations have been presented in earlier studies (e.g. Stier et al., 2005; Auvray et al., 2007; Pozzoli, 2008a,b,2011). All of these studies found good agreement between simulated and observed sulfate, black carbon and organic carbon surface concentrations in several world regions.

The simulations described in this study were performed using the coupled model ECHAM5-HAMMOZ with a spectral resolution of T42 corresponding to about 2.8×2.8 degrees in the horizontal dimension. The vertical resolution of the model is described by 31 hybrid σ -p levels from the surface up to 10 hPa, which corresponds to layer heights of ~ 50 m near the surface and

~1 km near the tropopause. Time step length was 20 minutes. In order to converge the model output obtained from free runs, we performed 8-member ensemble runs using AMIP sea surface temperature (SST) and sea ice cover (SIC) as lower boundary for the typical boreal summer season (June - September) of the year 2003, and each member starting from different initial conditions (from 24 to 31 March).

We compare two sets of results: (1) the base line simulations (CTRL) where the simulated aerosol concentrations are used in the calculation of the radiative budget and of the cloud droplet (CDNC, Lohmann et al. (1999), Lin and Leitch (1997)) and the ice crystal (ICNC Kaercher and Lohmann, 2002) concentrations; (2) the NOAER simulation where the standard ECHAM5 cloud scheme is used (Lohmann and Roeckner, 1996; Roeckner et al., 2003), without interactions between aerosols, radiative budget, cloud droplet and ice crystal concentrations. Precipitation formation in warm clouds, cold clouds and mixed phase clouds is discussed in details in the report 349 “The atmospheric general circulation model ECHAM 5, part-I” in section 10.3.4.

(http://www.mpimet.mpg.de/fileadmin/publikationen/Reports/max_scirep_349.pdf)

We analyze the difference between these two simulations CTRL – NOAER to quantify the influence of aerosols on temperature, water vapour, cloud ice, circulation and precipitation over the Asian region.

2.2 Satellite observations: SAGE II and HALOE

To evaluate the model results we have analyzed the distribution of aerosol extinction from two satellite based instruments: Stratospheric Aerosol and Gas Experiment II (SAGE II) aboard the Earth Radiation Budget Satellite (ERBS) and Halogen Occultation Experiment (HALOE) aboard the Upper Atmospheric Research Satellite (UARS). HALOE is a limb-viewing solar

occultation instrument that obtains transmittance profiles in the infra-red region of the spectrum giving 15 sunrise and 15 sunset measurements each day (Russell et al., 1993). HALOE was operational from September 1991 to November 2005. The vertical resolution is ~2 km or less. Measurements in eight infrared bands (2.45- 10.01 μm) are used to retrieve the profiles of seven trace gas mixing ratios (HCl, CH₄, HF, NO, NO₂, O₃, H₂O). Temperature and aerosols are retrieved at four wavelengths (2.45, 3.40, 3.46, 5.26 μm). The HALOE aerosol retrievals are described in detail by Hervig et al. (1995). The validation of these measurements suggests uncertainties of ~15-20% (Hervig et al., 1995). Aerosol extinction at 5.26 μm is analyzed to study transport of aerosols in the UTLS region. HALOE data are available at: <http://haloethree.larc.nasa.gov/download/>

SAGE II is also a solar occultation instrument where measurements are only made during limb viewing conditions providing 15 sunrise and 15 sunset measurements per day. During each sunrise and sunset encountered by the orbiting spacecraft, the instrument uses the solar occultation technique measuring the attenuated solar radiation through the Earth's limb in seven channels with central wavelengths ranging from 0.385 μm to 0.1020 μm . The transmittance measurements are inverted using the "onion-peeling" approach (Antuña et al., 2002) to retrieve the aerosol extinction coefficient (km^{-1}) as well as the other atmospheric compounds such as ozone, nitrogen dioxide, and water vapor at 0.385 μm , 0.453 μm , 0.525 μm , and 0.1020 μm . SAGE II has a horizontal resolution of the order of 200 km and a vertical resolution of 1 km (Kent et al., 1998). The SAGE II data used here are based on the v6.2 retrieval algorithm. SAGE II aerosol data has been validated by Oberbeck et al. (1989) indicating an extinction uncertainty of ~20-30%. Temporal and spatial coverage of HALOE are similar to those of SAGE II (Terao and Logan, 2007). To keep uniformity with HALOE aerosol extinction 5.26 μm , SAGE II

aerosol extinction data (km^{-1}) at $0.525 \mu\text{m}$ are analyzed. SAGE II data is available at:
[http://badc/sage2/data /version_6.2](http://badc/sage2/data/version_6.2).

3. Transport aerosols into the UTLS region due to ASM convection

In order to study the influence of ASM convection on the distribution of aerosols in the UTLS, monthly mean concentrations of black carbon (BC), sulfate (SO_4^{2-}), organic carbon (OC) and mineral dust aerosols from the ECHAM5-HAMMOZ ensemble are analyzed for the year 2003. These monthly mean aerosol concentrations (ng/m^3) are then averaged during ASM (June-September) to show seasonal average. Figure 1 shows the distributions of BC, SO_4^{2-} , OC, and mineral dust aerosol, respectively for the CTRL simulation at 110 hPa averaged during ASM 2003. Figure 1(a) also displays the average wind field at the same pressure level. The winds show a strong anticyclonic circulation between 20° - 120°E , 12° - 40°N collocated with a maximum in all aerosol fields. Confinement of aerosols within the anticyclonic circulation, with a pronounced maximum on its eastern part covering South-East Asia and India is quite obvious in Figures 1 (a)-(d).

To understand vertical transport, longitude-pressure and latitude-pressure cross-sections of the aerosol distribution in the anticyclonic region are analyzed. Figure 2 shows a longitude-pressure cross-section averaged over 15 - 35°N and for June-September as obtained from CTRL simulation. In agreement with satellite observations (Vernier et al 2011; Dodion et al., 2008) ECHAM5-HAMMOZ shows a layer of aerosols in the UTLS region (~between 416 hPa and 70 hPa). Transport of boundary layer aerosols from 60 - 120°E to the UTLS region due to large scale monsoon convection is evident. There are two regions of vertical transport eastward of 60°E , first at the eastern end of the anticyclone (around 85°E) and second around 120°E . This second region over the South China Sea is another pathway for aerosols into the UTLS and it is likely that some of this aerosol is transported westward by the equatorial easterly winds and is trapped in the anticyclone as identified by the aerosol maximum around 85°E and 110 hPa. The latitude-

pressure cross-sections (averaged over 60°E-120°E) of aerosol concentrations (BC, OC, SO₄²⁻ and mineral dust) averaged during the Asian monsoon season are plotted in Figure 3. Cross-tropopause transport (extending up to 70 hPa) is evident in all the aerosol distributions, but the details vary. Similar transport is observed during every month (June-September) for all the aerosol fields.

A pronounced maximum near 30°N is associated with the ASM anticyclone. High concentrations of BC, OC, SO₄²⁻ and mineral dust in the UTLS extend to the equator and are then transported poleward and downward in the southern hemisphere to ~30°S by the Brewer-Dobson circulation [thereby forming an arch](#). Most of the transport appears to occur [around](#) the tropical tropopause suggesting mixing by breaking Rossby waves in the lower tropical stratosphere and in the upper TTL. [This is consistent with the results of Homeyer and Bowman \(2013\) who find, using ECMWF ERA-Interim Reanalysis data, that there is strong equatorward transport in the Northern Hemisphere in JJAS by synoptic scale Rossby wave breaking near the 380 K isentropic surface.](#) Similar transport is also observed in ACE-FTS observations of HCN (Randel et al., 2010). From figures 2 and 3 one can also infer that large scale vertical transport within the anticyclone is related to deep monsoon convection over the region 10-35°N, 60-120°E. [Figure 2\(a\) shows vectors of the resolved circulation which exhibits a strong upwelling around 100°E.](#) This is a region of deep convection on the southern flanks of the Himalayas as can be seen from [Figure 4\(a\)-\(b\), which shows the combined distribution of Cloud Droplet Number Concentration \(CDNC\) and Ice Crystal Number Concentration \(ICNC\).](#) The upwelling shown in [Figure 2\(a\)](#) is induced by convective heating but does not represent the full transport experienced by aerosols and other tracers, which are subject to vertical redistribution by the sub-grid-scale deep convection parameterization. The distributions of the four aerosol species shown in [Figure 2](#) all

have a minimum between 180 and 270 hPa around 100°E with a distinct trench extending to below 500 hPa. The aerosol values increase above 180 hPa, which suggests deep convective transport extending above 180 hPa acting to remove aerosols from lower altitudes. The resolved circulation transports aerosols into the anticyclone core where they accumulate due to its confinement properties (Fig. 2(a)) so that the aerosol species maxima above 180 hPa occur between 80°E and 90°E. The convective activity over the Tibetan Plateau, that transports aerosols upward and poleward from 40°N (see figure 4(b)). This is a distinct convective transport pathway from the one described in the previous paragraph which occurs between 15°N and 35°N.

From Figure 3 it is apparent that aerosols accumulate around the extratropical tropopause and it is likely that large scale Rossby wave mixing processes are acting to transport some of these aerosols towards the equator (e.g. Homeyer and Bowman, 2013; Scott and Cammas, 2002).

The aerosol arch feature in the tropical tropopause region seen in Figure 3 cannot be explained by direct convective transport. Overshooting convection accounts for only about 5% of the total deep convective activity in the tropics, including the ASM region (Alcala and Dessler, 2002). Most convection does not penetrate above the zero diabatic heating surface at about 15 km (e.g. Folkins and Martin, 2005). The transport of water and hence aerosols to 100 hPa and above between 20°N and 40°N is achieved via large scale transport in the ASM anticyclone (James et al., 2008; Gettelman et al., 2004) and this is the primary channel for injection into the lower stratosphere. As noted above, transport by synoptic scale Rossby wave breaking towards the equator from the subtropics occurs around the 380 K isentrope in summer and fall. Mixing near the equator can occur through Kelvin waves (Fujiwara et al., 1998) and gravity waves (Moustaoui et al., 2004). Transport by synoptic scale Rossby wave breaking near 380 K in the

southern hemisphere during JJAS occurs both poleward and equatorward in equal measure as found by Homeyer and Bowman (2013). This will result in mixing of aerosols crossing the equator towards the southern hemisphere subtropics.

Figure 5 shows emissions of black carbon, organic carbon, mineral dust and sulfur over the Asian region and surrounding area. Sulfur emissions are primarily from coal-fired power plants. Asia is one of the highest sulfur producing regions in the world (Vernier et al., 2011). The industrial and residential sectors emit BC and OC which are produced through incomplete combustion of coal and bio-fuel and also in wildland fires. These emissions are high over south west China and the Indo Gangetic Plain (IGP). Source regions of high mineral dust are in North Africa, the north-west China Taklimakan desert, part of Arabia, Iran and the shores of the Caspian Sea. The low level convergence during ASM may collect these pollutants from the aforementioned regions and deep convective activity lifts them upward. As can be seen in figures 2 and 3, transport of aerosols into the UTLS primarily occurs over the convective region (15-30°N, 60-120°E). As noted above a major route for this convective transport is over northern India on the southern flanks of the Himalayas. There is deep convective transport over the South China Sea region as well.

Altitude-latitude cross sections of aerosol extinction obtained from HALOE (5.26 μm) and SAGE II (0.525 μm) and ECHAM5-HAMMOZ CTRL (0.550 μm) simulations, averaged over longitudes 60°E-120°E and for the ASM season (of the year 2003) are shown in Figures 6(a)-(c), respectively. Since the number of profiles obtained from HALOE decreases rapidly at altitudes below 16 km, aerosol extinction is plotted over the altitudes 16-32 km. Figures 6(a)-(b) show evidence of enhanced aerosol concentrations in the lower stratosphere transported into the southern hemisphere across the equator with descent over the southern subtropics. There is an

arch feature in the aerosol distribution between 40°S and 15-20°N above 18 km which is clearly separated from the aerosols in the lower TTL. This feature is similar to the one found in the ECHAM5-HAMMOZ simulation (see Figure 6(c)). The extra aerosol features seen in the observations and not in the model in the lower TTL are likely due to a combination of sampling bias and under-representation of overshooting convection in the model due to the coarse resolution. In addition, we are comparing an ensemble average of free runs with observations. The free runs do not reproduce the observed state of the atmosphere and averaging obscures much of the fine structure of individual ensemble realizations. The purpose of the comparison done here is to highlight similarities with the large scale aerosol distribution and it should be treated as qualitative.

As the Asian summer monsoon transport of pollution occurs every year (Park et al., 2009; Kunze et al., 2010; Vernier et al., 2011), a similar distribution of aerosols is also observed in Atmospheric Chemistry Experiment (ACE) measurements for the year 2005 (see Figure 6 in Dodion et al., 2008). Dodion et al. (2008) reported that the observed aerosol layer indicates the presence of high subvisible cirrus clouds. They also observed a correlation of latitudinal variation of cirrus clouds with the seasonal variation of the Inter-tropical convergence zone (ITCZ), which suggests a dependence on aerosol redistribution.

Deep convection occurs frequently over the region spanned by 15-30°N and 60-120°E. Outgoing Long-wave Radiation (OLR) averaged over this region is an indicator of convective forcing; hence the OLR time series can be used as a proxy of monsoon convection (Randel and Park, 2006). Association of deep convection with aerosols in the UTLS is examined by observing simultaneously time variations of OLR and BC, OC and SO₄²⁻ aerosols at 110 hPa averaged over the central monsoon region (20-30°N, 60-120°E). Figure 7 illustrates the coupling

of deep convection with aerosol transport within the anticyclone. A 10-20 day periodicity in convection is evident in the aerosols. Time series of BC, OC and SO_4^{2-} aerosols mixing ratio show statistically significant (at 95% confidence level) anti-correlation greater than 0.5 with OLR, thus all the aerosols vary coherently with OLR. During the strongest deep convective event in late June aerosol concentrations abruptly increase and they remain relatively high during the monsoon season. A similar coherent variation with convection was observed in AIRS data for water vapour (Randel and Park, 2006) and in [Aura MLS retrievals for CO \(Park et al., 2007\)](#). This indicates that the model is able to qualitatively reproduce the influence of AMS convection on UTLS aerosols.

4. Impact of aerosols on the UTLS region

4.1 Impact of aerosols on clouds

Li et al. (2005) proposed that uplifted boundary layer aerosols trapped by the Tibetan anticyclone could enhance high altitude cloud formation and would have consequences for precipitation. From Microwave Limb Sounder (MLS) observations they showed evidence of elevated ice water content collocated with a pollution-generated CO maximum during the ASM. [Global ozone Monitoring by Occultation of Stars \(GOMOS\)](#) and [Atmospheric Chemistry Experiment-Fourier Transform Spectrometer \(ACE-FTS\)](#) measurements also showed the coexistence of an aerosol layer and sub-visual tropical cirrus clouds during 2004 and 2005 at an altitude of 15-17 km (Dodion et al., 2008). Spatial distribution of ECHAM5-HAMMOZ (CTRL runs) simulated Ice Cloud Water (ICW) and Ice Crystal Number Concentration (ICNC) at 110 hPa are shown in Figures 8(a)-(b). It shows high amounts ICW ($2-4 \text{ decigram/m}^2$) and ICNC ($0.8-4 \text{ mg}^{-1}$) at the eastern flank of the anticyclone. Figures 8(c) and 8(d) exhibit time average and latitude-pressure cross sections (averaged over $60^\circ\text{E}-120^\circ\text{E}$) of ICW and ICNC. Maxima in

ICW (50-70 decigram/m²) and ICNC (16-24 mg⁻¹) collocated with the aerosol maximum (Figure 1) indicate that transport of aerosol and water vapour rich air by ITCZ may enhance cloud ice formation in the northern hemisphere subtropics. In simulations using the NCAR-CAM3 model coupled to the IMPACT global model, Liu et al. (2009) reported that in a scenario where homogeneous freezing of sulfate particles dominates cirrus cloud formation, anthropogenic sulfate emissions resulted in an increase of ICNC $\sim 0.03\text{-}0.5\text{ cm}^{-3}$ in the UTLS region of over the northern subtropics. The ECHAM5-HAMMOZ simulated ICNC over this region is $\sim 0.4\text{-}8\text{ cm}^{-3}$ (figure 8d). The ICNC as obtained ECHAM5-HAMMOZ is higher than that of Liu et al (2009). This may be due to differences in averaging over different areas and for time of the year. In the present study ICNC are averaged over the anticyclone area and for the ASM season while distribution of ICNC reported by Liu et al (2009) is annual average and zonal cross section across the globe.

High amounts of ICW and ICNC near the tropical tropopause layer indicate that uplifted boundary layer aerosols trapped by the Tibetan anticyclone may elevate cloud ice formation. The distribution of ICW and ICNC in this region is consistent with the aerosol distributions shown in Figures 3 and 6. High amounts of ICW and ICNC at lower latitudes are related to deep convection partly over the Indian Ocean and partly over south-east Asia and the Indonesian archipelago. So the ICW and ICNC concentrations between 10°-20°N are related to the ASM.

Processes in the UTLS have an impact on the radiative and chemical balance of the atmosphere. The difference between CTRL and NOAER simulations (aerosol induced anomalies) is shown in Figures 9-11. Figure 9(a) shows the horizontal distribution of the aerosol induced cloud ice ($\mu\text{g}/\text{m}^3$) anomalies at 181 hPa averaged during the ASM season. It shows a

prominent feature at the eastern end of the anticyclone region where the positive cloud ice anomaly has a maximum $\sim 15 \text{ mg/m}^3$. Figure 9(b) shows the time (ASM) and zonal average (60°E - 120°E) latitude versus pressure cross section of aerosol induced cloud ice anomalies ($\mu\text{g/m}^3$). It can be seen that cloud ice shows increases up to $10 \mu\text{g/m}^3$ near the tropical tropopause due to aerosol loading. Based on present day and pre-industrial scenarios, Liu et al. (2009) also reported an increase in aerosol induced (sulfate and black carbon) cloud ice anomalies (0 - 0.6 mg/kg) in the tropical upper troposphere. ECHAM5-HAMMOZ simulated cloud ice anomalies the tropical upper troposphere varies between 0 - 6 mg/kg . As stated above, these differences may be due to differences in averaging over different areas and for different time of the year.

Figure 9(b) shows cloud ice increase around 20°N which connects the lower troposphere to the upper troposphere and is associated with a region of enhanced vertical transport (see Figure 4). Increases of cloud ice near the tropical tropopause are associated with warming due to increased reflection of upwelling infrared radiation by cirrus clouds. Lau et al. (2006) and Lau and Kim (2006) reported that radiative heating of absorbing aerosols (mineral dust and BC) may cause upper tropospheric warming over the Tibetan Plateau during Asian summer monsoon season. The radiative heating from subvisible cirrus clouds near the tropopause can act to increase water vapour entering the stratosphere by increasing tropopause temperatures (Rosenfield et al., 1998). However, this effect is not captured here as subvisible cirrus clouds are not parameterized in the model.

4.2 Impact of aerosols on temperature, water vapour and circulation

Figures 10(a)-(c) show the aerosol induced change in the temperature and water vapour. The change in the meridional circulation and vertical upwelling are shown as well. There is an

increase in temperature ($\sim 1-5$ K) near the tropical tropopause. A similar increase in temperature is reported by Lau et al. (2006), Lau and Kim (2006), Liu et al. (2009), and Su et al. (2011). The interior of the anticyclone over the Tibetan plateau experiences a significant warming as well but the warming is greater than that found by Lau et al. (2006).

The aerosol induced meridional circulation anomaly shows descent (or decreased ascent) at about $0-10^{\circ}\text{N}$ and $35-40^{\circ}\text{S}$ (Figure 10(b)). This pattern indicates a slight contraction and weakening of the dominant Hadley circulation cell which straddles the equator. A weakening of the Hadley circulation due to aerosol forcing is consistent with the findings of Ramanathan et al. (2005) and Bollasina et al. (2011) although there are significant differences in the model scenarios being considered. Weaker upwelling in the ITCZ around 5°N is associated with reduced water vapour transport into the middle troposphere and warmer temperatures at the cold point due to lower cloud top heights. It also produces a cooling around 7 km and 5°N from reduced release of latent heat by cloud condensate.

A weak descent anomaly at the tropical tropopause is seen in Figure 10. This reduction in upwelling through the tropical tropopause is partly associated with the temperature increase seen in Figure 10(a). This feature is likely due to aerosol induced changes in the Brewer-Dobson circulation in the low latitude UTLS. The region of warming in the stratosphere above the tropical tropopause can influence wave propagation and dissipation. There are also significant dynamical changes in the NH subtropics associated with the ASM that are likely modifying the synoptic-scale Rossby wave flux (see discussion below).

The results presented here broadly agree with the transport picture presented by Fu et al. (2006) in that the primary route for tracers into the tropical tropopause layer (TTL) in the ASM region is via the convective zone on the southern flanks of the Himalayas. A prominent feature

seen in Figure 10 is the increase in vertical transport over this region. Air masses from the boundary layer reach the TTL and penetrate into the stratosphere. A large fraction of this circulation increase results from aerosol induced enhancement of convection. However, the circulation increase above 200 hPa seen in Figure 10 cannot be simply attributed to a change in the anticyclone. The zonal average over 90-110°E (not shown) shows that the tropopause is elevated noticeably over the region of increased convective activity on the southern flank of the Himalayas. This indicates that convection is extending above 200 hPa in this region.

The tropopause height increase can also be attributed in part to an intensification of the Brewer-Dobson circulation evident in Figure 10, which exhibits increased poleward and downward transport in the subtropics that has to be balanced by more tropical upwelling (Fig. 10(c)). This regional Brewer-Dobson circulation anomaly produces peak upwelling and downwelling over 0.3 mm/s which is significant (Mote et al., 1998) and facilitates the entry of tropospheric constituents into the lower tropical stratosphere. The increased Brewer-Dobson circulation implies an increase in wave drag. From the change in the zonal wind (not shown) it appears that both orographic gravity wave drag and synoptic scale Rossby wave drag have been modified due to aerosols. The former is due to an increase in the surface westerlies over India and the latter is due to an intensification of the subtropical jet and the associated change in vertical shear (e.g. Garcia and Randel, 2008). Previous studies indicate that parameterized non-orographic gravity wave drag plays a role in tropical upwelling in response to subtropical jet changes (McLandress and Shepherd, 2009; Calvo et al., 2010).

The meridional circulation anomaly between the equator and 30°N in the troposphere seen in Figure 10 can be interpreted as the result of increased convective heating over the southern flanks of the Himalayas around 100°E and between 20-25°N. It drives a thermal circulation (like

the Hadley circulation) and is subject to the same asymmetry that is discussed by Lindzen and Hou (1988). Namely that a localized heating anomaly centered off the equator but still in the tropics has a two-cell circulation pattern with a dominant circulation cell on the equatorward side. The intensification of this secondary circulation contributes to the decreased ascent around 5°N. It should be noted that the change in the Hadley circulation induced by aerosols is small and there is no significant change in its spatial structure.

Although the convective transport pathway in the CTRL simulations is distinct from that identified by Park et al. (2009), being centered on the southern flanks of the Himalayas, there is some agreement with their results. From the circulation pattern shown in Figure 4(a) it is clear that there is large scale, resolved upward and westward flow from the region eastward of 100°E which is penetrating inside the ASM anticyclone in the upper troposphere (delineated by the white contour in Fig. 2(a)). The region of the convective upwelling anomaly also extends to 15°N which overlaps the region spanning the Bay of Bengal and South-East Asia. Therefore it is possible for aerosol and trace gas species to enter the anticyclone from this region in agreement with the results of Park et al. (2009).

Figure 10(a) also shows a cold stratospheric temperature anomaly above a warm tropospheric temperature anomaly around 30-40°N and 30-40°S. This structure is a manifestation of a “Gill-type solution” identified by Park et al. (2007) where two anticyclonic vortices on both sides of the equator are induced by a near equatorial heat source, from deep convection, lying to the east. Analysis of the CTRL – NOAER geopotential and horizontal circulation difference at 100 hPa for June-September in our simulations (not shown) identifies two positive anomalies corresponding to a weaker anticyclone in the SH which mirrors a stronger anticyclone in the NH. Aerosols amplify the anticyclonic circulation in both

hemispheres by intensifying deep convective heating in the regions of the ASM and north of Indonesia.

Warming of the tropical cold point tropopause seen in the present study agrees with a geo-engineering study by Heckendorn et al. (2009) which demonstrated that continuous emission of sulfur into the tropical lower stratosphere would lead to increased cold point temperatures. Warming of this sensitive region would then induce moistening of the stratosphere which is apparent in Figure 10(b).

To further diagnose the impact of aerosols on UTLS vapor we analyzed water vapour anomalies as obtained from difference between CTRL and [NOAER](#) simulations at different pressure levels. Figures 11(a)-(e) show water vapor anomalies at 155 hPa, 132 hPa, 110 hPa, 90 hPa and 70 hPa, respectively. There are positive water vapor anomalies (0.2-3 ppmv) in the ASM anticyclone throughout the UTLS region induced by aerosols. Using the CAM3 climate model, Liu et al. (2009) demonstrated that increasing sulfate and soot pollution lead to increases in lower stratospheric water vapour ~ 0.3 ppmv(10%) and ~ 0.6 ppmv(20%), respectively. These results are in agreement with the present study. Above the tropopause there is a noticeable increase in water vapor between the equator and 15°N (Fig. 11(d)). This structure appears to be a horizontal transport feature the source of which is moisture injected into the lower tropical stratosphere over the South China Sea as well as northern India and the Himalayas. Figure 11(c) shows that this feature is not transported from below. From Figures 11(a)-(e) it is clear that aerosol enhances transport of water vapor into the lower stratosphere through the northern edge of the tropical tropopause inside the ASM anticyclone.

4.3 Impact of aerosols on precipitation

Figure 11 (f) shows the distribution of aerosol induced changes in precipitation (averaged over the ASM). There are negative precipitation anomalies (-1 to -3 mm/day) to the south of India and extending northward along its eastern half. There is a small decrease over northern India and the Tibetan plateau west of 90°E (about -1 mm/day). This feature is most likely due to weakening of Hadley circulation as indicated in Figure 10. The positive precipitation anomalies (0-3 mm/day) are over western India which extends across to the north-east around 20°N. At the eastern end of the anticyclone region (90-100°E and 12-30°N) there is significant increase in precipitation anomalies in the range of 5-7 mm/day. The positive vertical upwelling anomaly seen in Figure 10 around 20°N is most intense between 90°E and 100°E and is associated with the increased convection indicated by this precipitation anomaly. The weakening of the Hadley circulation applies to both the primary branch and the weak northern branch. This helps to intensify the convective system in question since the upwelling increases. However, aerosols are modifying the convection as well so the increase in the secondary thermally direct circulation at the base of the Himalayas is not due just to changes in the Hadley circulation. As with the Hadley circulation there is a feedback from the non-local thermally direct circulation onto the convection, intensifying it through increased vertical upwelling. The region of increased precipitation also extends over the South China Sea (1-3 mm/day). Simultaneous analysis of aerosol induced circulation changes (in Figure 10(a, b)) and precipitation changes (in Figure 10(f)) shows increased precipitation anomalies over the region of strong convection 15-30°N. Negative precipitation anomalies are observed in the region of reduced upwelling (5-10°N). However Lau et al. (2006) reported that rainfall response is not just a direct response to local aerosol forcing, but rather the result of a large scale dynamical adjustment to aerosol initiated

horizontal and vertical heating gradients to the atmosphere and land surface, modulating the climatological seasonal heating in spring and summer. So the impact of aerosols during ASM on precipitation requires a more comprehensive analysis which is beyond the scope of this study.

5. Conclusions

An Eight member ensemble of ECHAM5-HAMMOZ simulations a typical boreal summer season is analyzed to study the transport of aerosols during Asian summer monsoon in the UTLS. Simulations show persistent maxima in black carbon, organic carbon, sulfate, and mineral dust aerosols within the anticyclone in the UTLS throughout summer. Model simulations indicate the transport of boundary layer aerosol pollutant by ASM convection to the UTLS. The ASM transport of aerosols into the TTL and the lower tropical stratosphere is observed in HALOE and SAGE II aerosol extinction. Model simulations and satellite data shows that high concentrations of BC, OC, SO_4^{2-} and mineral dust around the tropical tropopause extend to low latitudes and are transported across the equator poleward and downward in the southern hemisphere to $\sim 30^\circ\text{S}$. Variations in all four types of aerosols in the anticyclone are closely related to deep convection.

Maxima in Ice cloud Water (ICW) and Ice Crystal Number Concentration (ICNC) collocated with aerosol maxima indicate that transport of aerosol and water vapour rich air by deep convection may enhance high level cloud ice formation in the northern hemisphere subtropics. Changes in cloud properties have an impact on the hydrological cycle and climate. These aspects require more detailed analysis which is beyond the scope of this study.

The impact of aerosols in the UTLS region is analyzed by computing differences between the CTRL and NOAER simulations. Transport of anthropogenic aerosols into the UTLS produces a complex response in temperature, water vapour and cloud ice in this region. There is warming of the tropical tropopause and the lower tropical stratosphere which is associated with direct and indirect effects of aerosols on transport and dynamics. A notable feature is the increased vertical transport between $15\text{-}30^\circ\text{N}$ and around 100°E , which reaches into the tropical

lower stratosphere. This is the primary transport pathway into the TTL and tropical lower stratosphere and agrees with the observational findings of Fu et al. (2006) that the southern slopes of the Himalayas are the region with the deepest penetrating convection. However, the convective region from the Bay of Bengal to the South China Sea is also a source of aerosols given the structure of the large scale circulation in agreement with the pathway identified by Park et al. (2009). In addition to convection and the associated diabatic circulation change in the troposphere, the transport change in this region involves the stratospheric Brewer-Dobson circulation near the tropopause. There is a significant increase in cross-tropopause transport between 15°N and 35°N.

Aerosols induce a weakening of the Hadley circulation, as noted in previous studies (e.g. Ramanathan et al., 2005; Bollasina et al., 2011), and an intensification of a secondary thermally direct circulation associated with the region of strong convection on the southern flanks of the Himalayas (15-30°N and around 100°E). The effect is to reduce vertical upwelling around 5°N, which reduces transport of water vapour into the mid troposphere near the equator. At the same time there is increased transport of water vapour around 15-30°N. Significant positive precipitation anomalies (5-7 mm/day) are observed over the region of intensified convection, at the eastern end of the anticyclone (90-100°E). There are negative precipitation anomalies (-1 to -3 mm/day) to the south of India and extending northward along its eastern half. There is a small decrease over northern India and the Tibetan plateau west of 90°E (about -1 mm/day). Negative precipitation anomalies are collocated with reduced upwelling around 5-10°N. This is most likely due to weakening of Hadley circulation upwelling at these latitudes. The impact of aerosols on precipitation requires a more detailed study to be done later.

Cirrus clouds play an important role in climate (Liou, 1986). Thin cirrus clouds were an uncertain component which has been recently found to be a significant fraction of the total cirrus distribution (e.g. Lee et al., 2009). Hence, anthropogenic aerosols transported by ASM convection to the UTLS region may impact the hydrological cycle and climate. Several studies (e.g. Randall et al., 1989; Ramaswamy and Ramanathan, 1989; Liu et al., 2003a,b) point out that cirrus clouds are likely to have great impact on the radiation and hence the intensity of the large-scale circulation in the tropics. In particular, some studies (Su et al., 2011) suggest that pollution acts to warm the TTL and could lead to a moistening of the stratosphere. In agreement with these studies our simulations shows increase in tropical tropopause temperature by 0.3-2.5 K and an associated increase water vapor 0.2-3 ppmv.

Acknowledgements

S. Fadnavis acknowledge with gratitude Prof. B. N. Goswami, Director IITM for his encouragement during the course of this study. The authors thank SAGE II and HALOE team for providing data and the High Power Computing Center (HPC) in IITM, Pune, India for providing computer resources. We thank anonymous reviewers for their useful comments that helped to improve the manuscript.

References

- Alcala, C. M., and Dessler, A. E.: Observations of deep convection in the tropics using the TRMM precipitation radar, *J. Geophys. Res.*, 107(D24), 4792, doi:10.1029/2002JD002457, 2002.
- Antuña, J. C., Robock, A., Stenchikov, G. L., Thomason, L. W., and Barnes, J. E.: Lidar validation of SAGE II aerosol measurements after the 1991 Mount Pinatubo eruption, *J. Geophys. Res.*, 107, 4194, doi:10.1029/2001JD001441, 2002.
- Auvray, M., Bey, I., Lull, E., Schultz, M. G., and Rast, S.: A model investigation of tropospheric ozone chemical tendencies in long-range transported pollution plumes, *J. Geophys. Res.*, 112, D05304, doi:10.1029/2006JD007137, 2007.
- Bollasina, M. A., Ming, Y., and Ramaswamy, V.: Anthropogenic Aerosols and the Weakening of the South Asian Summer Monsoon, *Science*, 334, 6055, 502-505, doi:10.1126/science.1204994, 2011.
- Calvo, N., Garcia, R. R., Randel, W. J., and Marsh, D.: Dynamical mechanism for the increase in tropical upwelling in the lowermost tropical stratosphere during warm ENSO events. *J. Atmos. Sci.*, 67, 2331-2340, doi: 10.1175/2010JAS3433.1, 2010.
- Chen, B., Xu, X. D., Yang, S., and Zhao, T. L.: Climatological perspectives of air transport from atmospheric boundary layer to tropopause layer over Asian monsoon regions during boreal summer inferred from Lagrangian approach, *Atmos. Chem. Phys.*, 12, 5827–5839, 2012.
- Cheng, T., Peng, Y., Feichter, J., and Tegen, I.: An improvement on the dust emission scheme in the global aerosol-climate model ECHAM5-HAM, *Atmos. Chem. Phys.*, 8, 1105–1117, doi:10.5194/acp-8-1105-2008, 2008.
- Dentener, F., Kinne, S., Bond, T., Boucher, O., Cofala, J., Generoso, S., Ginoux, P., Gong, S., Hoelzemann, J. J., Ito, A., Marelli, L., Penner, J. E., Putaud, J.-P., Textor, C., Schulz, M., van der Werf, G. R., and Wilson, J.: Emissions of primary aerosol and precursor gases in the years 2000 and 1750 prescribed data-sets for AeroCom, *Atmos. Chem. Phys.*, 6, 4321–4344, 2006.

- Dodion, J., Fussen, D., Vanhellefont, F., Bingen, C., Matshvili, N., Gilbert, K., Skelton, R., Turnball, D., McLeod, S. D., Boone, C. D., Walker, K. A., and Bernath P. F.: Aerosols and clouds in the upper troposphere-lower stratosphere region detected by GOMOS and ACE: Intercomparison and analysis of the years 2004 and 2005, *Adv. Space Res.*, 42, 1730-1742, doi:10.1016/j.asr.2007.09.027, 2008.
- Folkens, I., and Martin, R. V.: The Vertical Structure of Tropical Convection and Its Impact on the Budgets of Water Vapor and Ozone. *J. Atmos. Sci.*, 62, 1560–1573, doi: 10.1175/JAS3407.1, 2005.
- Fu, R., Hu, Y., Wright, J. S., Jiang, J. H., Dickinson, R. E., Chen, M., Filipiak, M., Read, W. G., Waters, J.W., and Wu, D. L.: Short circuit of water vapor and polluted air to the global stratosphere by convective transport over the Tibetan Plateau, *Proc Natl Acad Sci U S A*. Apr 11, 103(15), 5664-9, Epub Apr 3, 2006.
- Fujiwara, M., Kita, K., and Ogawa, T.: Stratosphere-troposphere exchange of ozone associated with the equatorial Kelvin wave as observed with ozonesondes and rawinsondes. *J. Geophys. Res.*, 103, 19173–19182, doi: 10.1029/98JD01419, 1998.
- Garcia, R. R., and Randel, W. J.: Acceleration of the Brewer–Dobson circulation due to Increases in greenhouse gases., *J. Atmos. Sci.*, 65, 2731–2739, doi:10.1175/2008JAS2712.1, 2008.
- Gettelman, A., Kinnison, D. E., Dunkerton, T. J., and Brasseur, G. P.: The impact of monsoon circulations on the upper troposphere and lower stratosphere, *J. Geophys. Res.*, 109, D22101, doi:10.1029/2004JD004878, 2004.
- Guenther, A., Karl, T., Harley, P., Wiedinmyer, C., Palmer, P. I., and Geron, C.: Estimates of global terrestrial isoprene emissions using MEGAN (Model of Emissions of Gases and Aerosols from Nature), *Atmos. Chem. Phys.*, 6, 3181–3210, doi:10.5194/acp-6- 3181-2006, 2006.
- Grewe, V., Brunner, D., Dameris, M., Grenfell, J. L., Hein, R., Shindell, D., and Staehelin, J.: Origin and variability of upper tropospheric nitrogen oxides and ozone at northern mid-latitudes, *Atmos. Environ.*, 35, 3421–3433, 2001.

- Heckendorn, P., Weisenstein, D., Fueglistaler, S., Luo, B. P., Rozanov, E., Schraner, M., Thomason, L. W., and Peter, T.: The impact of geoengineering aerosols on stratospheric temperature and ozone, *Environ. Res. Lett.*, 4, 045108, doi:10.1088/1748-9326/4/4/045108, 2009.
- Hervig, M. E., Russell III, J. M., Gordley, L. L., Daniels, J., Drayson, S. R., and Park, J. H.: Aerosol effects and corrections in the Halogen Occultation Experiment, *J. Geophys. Res.*, 100, 1067–1079, 1995.
- Homeyer, C. R., and Bowman, K. P.: Rossby wave breaking and transport between the tropics and extratropics above the subtropical jet, *J. Atmos. Sci.*, 70, 607–626, doi:10.1175/JAS-D-12-0198.1, 2013.
- Horowitz, L. W., Walters, S., Mauzerall, D. L., Emmons, L. K., Rasch, P. J., Granier, C., Tie, X., Lamarque, J., Schultz, M. G., Tyndall, G. S., Orlando, J. J., and Brasseur, G. P.: A global simulation of tropospheric ozone and related tracers: Description and evaluation of MOZART, version 2, *J. Geophys. Res.*, 108(D24), 2003.
- IPCC (Intergovernmental Panel on Climate Change): *Climate Change 2007 - The Physical Science Basis, Contribution of Working Group 1 to the Fourth Assessment Report of the Intergovernmental Panel on Climate Change*, Cambridge University Press, Cambridge, UK and New York, 2007.
- James, R., Bonazzola, M., Legras, B., Surbled, K., and Fueglistaler, S.: Water vapor transport and dehydration above the convective outflow during Asian monsoon, *Geophys. Res. Lett.*, 35, L20810, doi:10.1029/2008GL035441, 2008.
- Jeong, J. I., Park, R. J., Woo, J. H., Han, Y. J., and Yi, S. M.: Source contributions to carbonaceous aerosols in Korea. *Atmos. Environ.*, 45, 1116-1125. 2011.
- Kaercher, B., and U. Lohmann, A parameterization of cirrus cloud formation: Homogeneous freezing of supercooled aerosols, *J. Geophys. Res.*, 107(D1), 10.1029/2001JD000470, 2002.

- Kent, G. S., Trepte, C. R., Skeens, K. M., and Winker, D. M.: LITE and SAGE II measurements of aerosols in the southern hemisphere upper troposphere, *J. Geophys. Res.*, 103(D15), 19,111–19,127, doi:10.1029/98JD00364, 1998.
- Kettle, A. and Andreae, M.: Flux of dimethylsulfide from the oceans: A comparison of updated data seas and flux models, *J. Geophys. Res.-Atmos.*, 105, 26793–26808, 2000.
- Kinnison, D. E., Brasseur, G. P., Walters, S., Garcia, R. R., Marsh, D. R., Sassi, F., Harvey, V. L., Randall, C. E., Emmons, L., Lamarque, J. F., Hess, P., Orlando, J. J., Tie, X. X., Randel, W., Pan, L. L., Gettelman, A., Granier, C., Diehl, T., Niemeier, U., and Simmons, A. J.: Sensitivity of chemical tracers to meteorological parameters in the MOZART-3 chemical transport model, *J. Geophys. Res.*, 112, D20302, doi:10.1029/2006JD007879, 2007.
- Kravitz, B., Robock, A., Shindell, D. T., and Miller, M.A.: Sensitivity of stratospheric geoengineering with black carbon to aerosol size and altitude of injection. *J. Geophys. Res.*, 117, D09203, doi:10.1029/2011JD017341, 2012.
- Kunze, M., Braesicke, P., Langematz, U., Stiller, G., Bekki, S., Brühl, C., Chipperfield, M., Dameris, M., Garcia, R., and Giorgetta, M.: Influences of the Indian Summer Monsoon on Water Vapor and Ozone Concentrations in the UTLS as Simulated by Chemistry–Climate Models. *J. Climate*, 23, 3525–3544, 2010.
- Lau, K. M., and Kim, K. M.: Observational relationships between aerosol and Asian monsoon rainfall, and circulation, *Geophys. Res. Lett.*, 33, L21810, doi:10.1029/2006GL027546, 2006.
- Lau, K. M., Kim, M. K. and Kim, K. M.: Asian summer monsoon anomalies induced by aerosol direct forcing: the role of the Tibetan Plateau, *Climate Dynamics*, Volume 26, Issue 7-8, pp. 855-864, 2006.
- Lee, J., Yang, P., Dessler, A. E., Gao, B.-C., and Platnick, S.: Distribution and radiative forcing of tropical thin cirrus clouds. *J. Atmos. Sci.*, 66, 3721–3731, doi: 10.1175/2009JAS3183.1, 2009.

- Li, Q., Jiang, J. H., Wu, D. L., Read, W. G., Livesey, N. J., Waters, J. W., Zhang, Y., Wang, B., Filipiak, M. J., Davis, C. P., Turquety, S., Wu, S., Park R. J., Yantosca R. M., and Jacob D. J.: Convective outflow of South Asian pollution: A global CTM simulation compared with EOS MLS observations, *Geophys. Res. Lett.*, 32, L14826, doi:10.1029/2005GL022762, 2005.
- Liou, K-N.: Influence of cirrus clouds on weather and climate processes: A global perspective. *Mon. Wea. Rev.*, 114, 1167–1199, 1986.
- Lin, H., and Leitch, R.: Development of an in-cloud aerosol activation parameterization for climate modelling, in: Proc. WMO Workshop on Measurements of Cloud Properties for Fore- casts of Weather, Air Quality and Climate, Mexico City, 13562, 13563, 13602, 1997.
- Lindzen, R. S., and Hou, A.Y.: Hadley circulations for zonally averaged heating centered off the equator. *J. Atmos. Sci.*, 45, 2416-2427, 1988.
- Liu, H. L., Wang, P. K., and Schlesinger, R. E.: A numerical study of cirrus clouds. Part I: Model description, *J. Atmos. Sci.*, 60(8),1075– 1084, 2003a.
- Liu, H. L., Wang, P. K., and Schlesinger, R. E.: A numerical studyof cirrus clouds. Part II: Effects of ambient temperature, stability, radiation, ice microphysics, and microdynamics on cirrus evolution, *J. Atmos. Sci.*, 60(9), 1097– 1119, 2003b.
- Liu, J., and Diamond, J.: China’s Environment in a Globalizing World. *Nature*. 435(June 30), 1179-1186, 2005.
- Liu, X., Penner, J. E., and Wang M.: Influence of anthropogenic sulfate and black carbon on upper tropospheric clouds in the NCAR CAM3 model coupled to the IMPACT global aerosol model, *J. Geophys. Res.*, 114, D03204, doi:10.1029/2008JD010492, 2009.
- Logan, J.: An analysis of ozonesonde data for the troposphere: Recommendations for testing 3-D models and development of a gridded climatology for tropospheric ozone, *J. Geophys. Res.*, 104(D13), 16,115–16,149, 1999.

- Lohmann, U., and Roeckner, E.: Design and performance of a new cloud microphysics scheme developed for the ECHAM general circulation model, *Climate Dynamics*, 12, 557–572, 1996.
- Lohmann, U., Feichter, J., Chuang, C. C., and Penner, J. E.: Prediction of the number of cloud droplets in the ECHAM GCM, *J. Geophys. Res.*, 104(D8), 9169–9198, doi:10.1029/1999JD900046, 1999.
- McLandress, C. and Shepherd, T. G.: Simulated Anthropogenic Changes in the Brewer–Dobson Circulation, Including Its Extension to High Latitudes. *J. Climate*, 22, 1516–1540, doi: 10.1175/2008JCLI2679.1, 2009.
- Menon, S., Hansen, J., Nazarenko, L., and Luo, Y.: Climate effects of black carbon aerosols in China and India. *Science* 297:2250–2253, 2002.
- Moustaoui, M., Joseph, B., and Teitelbaum, H.: Mixing layer formation near the tropopause due to gravity wave-critical level interactions in a cloud-resolving model, *J. Atmos. Sci.*, 61, 3112–3124, doi: 10.1175/JAS-3289.1, 2004.
- Nightingale, P., Malin, G., Law, C., Watson, A., Liss, P., Liddicoat, M., Boutin, J., and Upstill-Goddard, R.: In situ evaluation of air-sea gas exchange parameterizations using novel conservative and volatile tracers, *Global Biogeochem. Cy.*, 14, 373–387, 2000.
- Oberbeck, V. R., Livingston, J. M., Russell, P. B., Pueschel, R. F., Rosen, J. N., Osborn, M. T., Kritz, M. A., Snetsinger, K. G., and Ferry, G. V.: SAGE II aerosol validation: Selected altitude measurements, including particle micrometeorology, *J. Geophys. Res.*, 94(D6), 8367–8380, doi:10.1029/JD094iD06p08367, 1989.
- Park M., Randel W. J., Gettleman, A., Massie, S. T., and Jiang, J. H.: Transport above the Asian summer monsoon anticyclone inferred from Aura Microwave Limb Sounder tracers, *J. Geophys. Res.*, 112, D16309, doi:10.1029/2006JD008294, 2007.
- Park, M., Randel, W. J., Emmons, L. K., and Livesey, N. J.: Transport pathways of carbon monoxide in the Asian summer monsoon diagnosed from Model of Ozone and Related Tracers (MOZART), *J. Geophys. Res.*, 114, D08303, doi:10.1029/2008JD010621, 2009.

- Park, M., Randel, W. J., Kinnison, D. E., Garcia, R. R., and Choi, W.: Seasonal variation of methane, water vapor, and nitrogen oxides near the tropopause: Satellite observations and model simulations, *J. Geophys. Res.*, doi:10.1029/2003JD003706, 109, D03302, 2004.
- Park, R. J., Kim, M. J., Jeong, J. I., Youn, D., and Kim, S.: A contribution of brown carbon aerosol to the aerosol light absorption and its radiative forcing in East Asia. *Atmos. Environ.*, 44, 1414-1421, 2010.
- Pham, M., Muller, J., Brasseur, G., Granier, C., and Megie, G.: A three-dimensional study of the tropospheric sulfur cycle, *J. Geophys. Res.-Atmos.*, 100, 26061–26092, 1995.
- Pozzoli, L., Bey, I., Rast, J. S., Schultz, M. G., Stier, P., and Feichter, J.: Trace gas and aerosol interactions in the fully coupled model of aerosol-chemistry-climate ECHAM5-HAMMOZ: 1. Model description and insights from the spring 2001 TRACE-P experiment, *J. Geophys. Res.*, 113, D07308, doi:10.1029/2007JD009007, 2008a.
- Pozzoli, L., Bey, I., Rast, J. S., Schultz, M. G., Stier, P., and Feichter, J.: Trace gas and aerosol interactions in the fully coupled model of aerosol-chemistry-climate ECHAM5-HAMMOZ: 2. Impact of heterogeneous chemistry on the global aerosol distributions, *J. Geophys. Res.*, 113, D07309, doi:10.1029/2007JD009008, 2008b.
- Pozzoli, L., Janssens-Maenhout, G., Diehl, T., Bey, I., Schultz, M. G., Feichter, J., Vignati, E., and Dentener, F.: Re-analysis of tropospheric sulfate aerosol and ozone for the period 1980–2005 using the aerosol-chemistry-climate model ECHAM5-HAMMOZ, *Atmos. Chem. Phys.*, 11, 9563-9594, doi:10.5194/acp-11-9563-2011, 2011.
- Ramanathan, V., Chung, C., Kim, D., Bettge, T., Buja, L., Kiehl, J. T., Washington, W. M., Fu, Q., Sikka, D. R., and Wild M.: Atmospheric Brown Clouds: Impacts on South Asian Climate and Hydrological Cycle. *PNAS*, 102, 15, 5326-5333, doi:10.1073/pnas.0500656102, 2005.
- Ramaswamy, V., and Ramanathan V.: Solar absorption of cirrus clouds and the maintenance of the tropical upper troposphere thermal structure, *J. Atmos. Sci.*, 46, 2293– 2310, 1989.

- Randall, D. A., Harshovardan, D. A. Dazlich, and Corsetti, T. G.: Interactions among radiation, convection, and large-scale dynamics in a general circulation model, *J. Atmos. Sci.*, 46, 1943–1970, 1989.
- Randel, W. J., and Park, M.: Deep convective influence on the Asian summer monsoon anticyclone and associated tracer variability observed with Atmospheric Infrared Sounder (AIRS), *J. Geophys. Res.*, 111, D12314, doi:10.1029/2005JD006490, 2006.
- Randel, W. J., Park, M., Emmons, L., Kinnison, D., Bernath, P., Walker, K. A., Boone, C., and Pumphrey H.: Asian monsoon transport of pollution to the stratosphere, *Science*. Apr 30, 328(5978), 611-3. Epub Mar 25, 2010.
- Randel, W., Wu, F., Russell, J., Roche, A., and Waters J.: Seasonal cycles and QBO variations in stratospheric CH₄ and H₂O observed in UARS HALOE data, *J. Atmos. Sci.*, 55(2), 163–185, 1998.
- Roeckner, E., Bauml, G., Bonaventura, L., Brokopf, R., Esch, M., Giorgetta, M., Hagemann, S., Kirchner, I., Kornbluh, L., Manzini, E., Rhodin, A., Schlese, U., Schulzweida, U., and Tompkins, A.: The atmospheric general circulation model ECHAM5: Part 1, Tech. Rep. 349, Max Planck Institute for Meteorology, Hamburg, 2003.
- Rosenfield, J. E., Considine, D. B., Schoeberl, M., and Browell, E.: The impact of subvisible cirrus clouds near the tropical tropopause on stratospheric water vapor, *Geophys. Res. Lett.*, 25, p. 1883, doi:10.1029/98GL01294, 1998.
- Russell, J. M., Gordley, L. L., Park, J. H., Drayson, S. R., Hesketh, W. D., Cicerone, R. J., Tuck, A. F., Frederick, J. E., Harries, J. E., Crutzen P. J.: The Halogen occultation Experiment. *Journal of Geophysical Research* 98, 10777-10797, 1993.
- Schultz, M., Heil, A., Hoelzemann, J., Spessa, A., Thonicke, K., Goldammer, J., Held, A., Pereira, J., and van het Bolscher, M.: Global wildland fire emissions from 1960 to 2000, *Global Biogeochem. Cycles*, *Global Biogeochemical Cycles*, 22, GB2002, 1-17., doi:10.1029/2007GB003031, 2008.
- Schulz, M., de Leeuw, G., and Balkanski, Y.: Emission of Atmospheric Trace Compounds, chap. Sea-salt aerosol source functions and emissions, 333–359, Kluwer, 2004.
- Scott, R. K., and Cammas, J.-P.: Wave breaking and mixing at the subtropical tropopause, *J. Atmos. Sci.*, 59, 2347-2361, doi:10.1175/1520-0469(2002)059, 2002.

- Stier, P., Feichter, J., Kinne, S., Kloster, S., Vignati, E., Wilson, J., Ganzeveld, T., Tegen, I., Werner, M., Balkanski, Y., Schulz, M., Boucher, O., Minikin, A., and Petzold, A.: The aerosolclimate model ECHAM5-HAM, *Atmos. Chem. Phys.* 5, 1125– 1165, doi:10.5194/acp-5-1125-2005, 2005.
- Su, H., Jiang, J. H., Liu, X., Penner, J. E., Read, W. G., Massie, S., Schoeberl, M. R., Colarco, P., Livesey, N. J., and Santee, M. L.: Observed increase of TTL temperature and water vapor in polluted clouds over Asia, *J. Climate*, 24, 2728–2736, doi:10.1175/2010JCLI3749.1, 2011.
- Tegen, I., Harrison, S., Kohfeld, K., Prentice, I., Coe, M., and Heimann, M.: Impact of vegetation and preferential source areas on global dust aerosol: Results from a model study, *J. Geophys. Res.-Atmos.*, 107, 4576, doi:10.1029/2001JD000963, 2002.
- Terao, Y., and Logan, J. A.: Consistency of time series and trends of stratospheric ozone as seen by ozonesonde, SAGE II, HALOE, and SBUV(2), *J. Geophys. Res.*, 112, D06310, doi:10.1029/2006JD007667, 2007.
- Venkataraman C., Habib, G., Eiguren-Fernandez, A., Miguel, A. H., and Friedlander, S. K.: Residential Biofuels in South Asia: Carbonaceous Aerosol Emissions and Climate Impacts *Science*, 307, 1454 , doi: 10.1126/science.1104359, 2005.
- Vernier, J. P., Thomason, L. W., and Kar, J.: CALIPSO detection of an Asian tropopause aerosol layer, *Geophys. Res. Lett.*, 38, L07804, doi:10.1029/2010GL046614, 2011.
- Vignati, E., Wilson, J., and Stier, P.: M7: An efficient size-resolved aerosol microphysics module for large-scale aerosol transport models, *J. Geophys. Res.*, 109, D22202, doi:10.1029/2003JD004485, 2004.
- Wild, M.: Global dimming and brightening: A review, *J. Geophys. Res.*, 114, D00D16, doi:10.1029/2008JD011470, 2009.
- WMO (World Meteorological Organization): *International Meteorological Vocabulary*, 2nd ed., 784 pp., Geneva, Switzerland, 1992.

- Xiong, X., Houweling, S., Wei, J., Maddy, E., Sun, F., and Barnet, C.: Methane plume over South Asia during the monsoon season: Satellite observation and model simulation, *Atmos. Chem. Phys.*, 9, 783–794, 2009.
- Yin, Y., Carslaw, K. S., and Feingold, G.: Vertical transport and processing of aerosols in a mixed-phase convective cloud and the feedback on cloud development, *Q. J. R. Meteorol. Soc.*, 131, 221–246, 2005.

Figure captions

- Figure 1. Horizontal structure of June-September 2003 averages at 110 hPa of aerosol concentrations (ng/m^3): (a) BC and horizontal wind fields (shown as vectors), (b) OC, (c) SO_4^{2-} and (d) mineral dust.
- Figure 2. Longitude–pressure section (averaged for June-September and $15\text{-}35^\circ\text{N}$) of concentrations (ng/m^3) of (a) BC aerosols, location of the monsoon anticyclone indicated with dotted line, (b) OC aerosols, (c) SO_4^{2-} and (d) Mineral dust aerosols. Vectors of the circulation are shown in (a) with the vertical wind scaled by 300. The upper black line marks the latitudinal averaged tropopause showing increased height in the ASM region. The lower black line marks the topography. The dashed white line is the negative 10^{-5} vorticity contour showing the approximate region of the anticyclone.
- Figure 3. Latitude–pressure section (averaged for June-September and $60\text{-}120^\circ\text{E}$) of concentrations (ng/m^3) of (a) BC aerosols, (b) OC aerosols, (c) SO_4^{2-} aerosols, (d) Mineral dust aerosols. The black line marks the longitudinally averaged tropopause showing increased height in the ASM region.
- Figure 4. Distribution of Cloud Droplet Number Concentration (CDNC) and Ice Crystal Number Concentration (ICNC) ($1/\text{mg}$) averaged for June-September 2003. (a) Latitude average between 20N and 30N and (b) zonal average between 60E and 120E .
- Figure 5. Distribution of emission mass flux ($\text{kg}/\text{m}^2/\text{s}$) averaged for June-September 2003 for (a) BC, (b) OC, (c) SO_4^{2-} , and (d) mineral dust.
- Figure 6. Latitude –pressure section (averaged for June-September and $60\text{-}120^\circ\text{E}$) of aerosol extinction (km^{-1}) as obtained from (a) HALOE $5.26\ \mu\text{m}$ for the year 2003 (b) SAGE II $0.525\ \mu\text{m}$ (c) ECHAM5-HAMMOZ simulations $0.550\ \mu\text{m}$ for the year 2003 at the altitude 16-32 km
- Figure 7. Time series of OLR (Wm^{-2}) averaged over ($15\text{-}30^\circ\text{N}$, $60\text{-}120^\circ\text{E}$) and ECHAM5-HAMMOZ simulated concentrations (ng/m^3) of BC, OC, SO_4^{2-} , averaged over $20\text{-}30^\circ\text{N}$ and $60\text{-}120^\circ\text{E}$. Note that the scale for OLR is inverted. The anti-correlation coefficient of BC, OC, SO_4^{2-} , with OLR is indicated at the top of the each panel.
- Figure 8. (a) Horizontal structure as obtained from ECHAM5-HAMMOZ CTRL simulations (averaged for ASM) of (a) cloud ice water ($\text{decigram}/\text{m}^2$) at 110 hPa (b) ice crystal number concentration ($1/\text{mg}$) at 110 hPa (c) Latitude-pressure cross section (averaged for June-September and $60\text{-}120^\circ\text{E}$) of cloud ice water ($\text{decigram}/\text{m}^2$) (d)

Latitude–pressure cross section (averaged for June–September and 60–120°E) of ice crystal number concentration (ICNC) (1/mg).

Figure 9. Spatial structure of mean cloud ice ($\mu\text{g}/\text{m}^3$) anomalies as obtained from ECHAM5-HAMMOZ CTRL – **NOAER** runs during ASM. (a) Pressure level slice at 181 hPa. (b) Latitude-pressure distribution averaged over 60–120°E.

Figure 10. Latitude-pressure structure (averaged over 60–120°E) of difference between ECHAM5-HAMMOZ CTRL - **NOAER** runs during ASM for (a) temperature (K), (b) water vapour (ppmv) and (c) vertical wind (mm/s, not scaled). The meridional circulation is shown as a vector field (the vertical velocity field has been scaled by 300 and the units are m/s).

Figure 11. (a) Spatial structure of mean water vapor (ppmv) anomalies obtained from ECHAM5-HAMMOZ CTRL – **NOAER** runs during ASM at (a) 155 hPa, (b) 132 hPa, (c) 110 hPa, (d) 90 hPa, (e) 70 hPa and (f) Spatial distribution of mean (JJAS) precipitation (mm/day) anomalies.

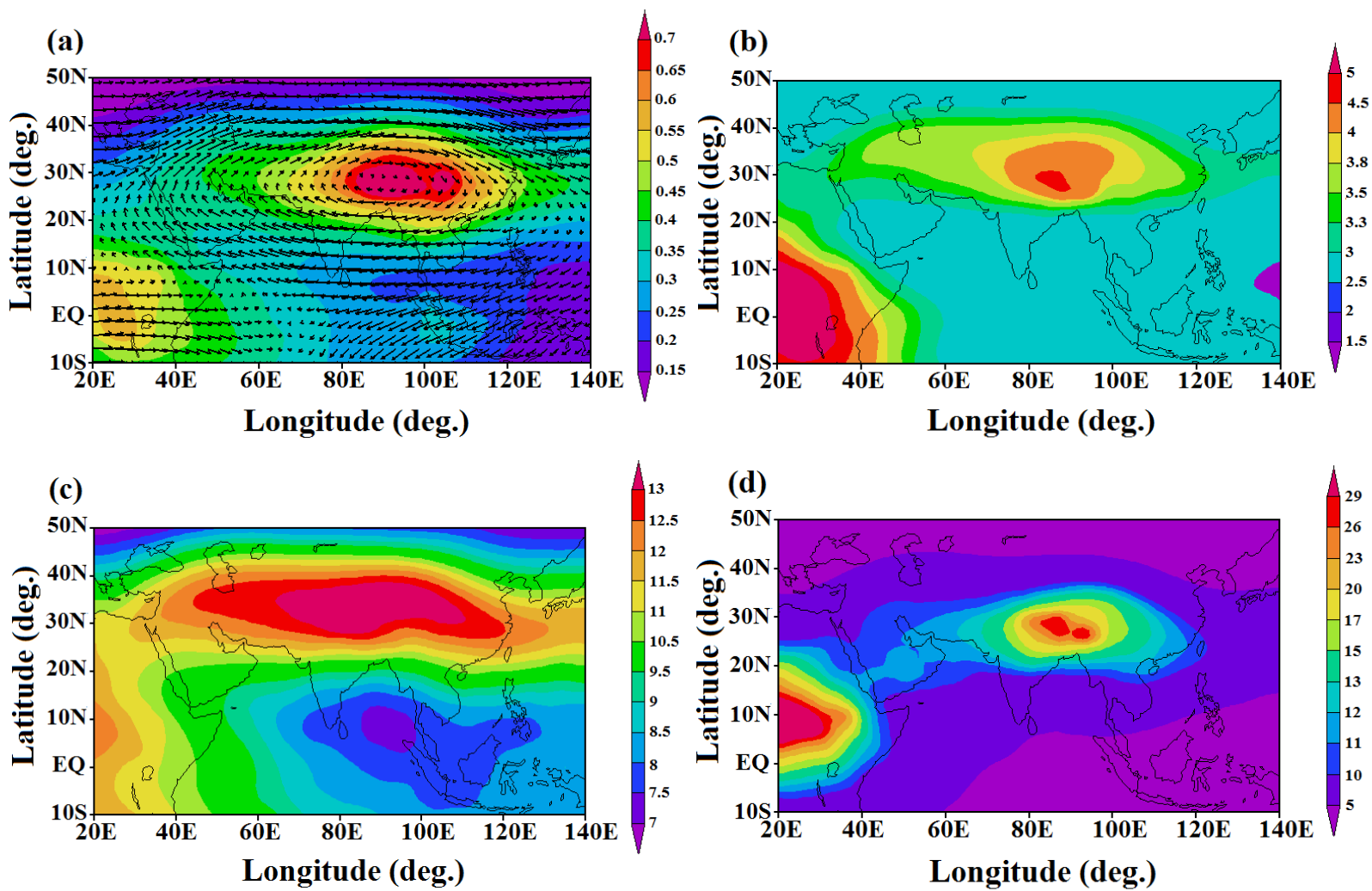


Figure 1. Horizontal structure of June-September 2003 averages at 110 hPa of aerosol concentrations (ng/m³): (a) BC and horizontal wind fields (shown as vectors), (b) OC, (c) SO₄²⁻ and (d) mineral dust.

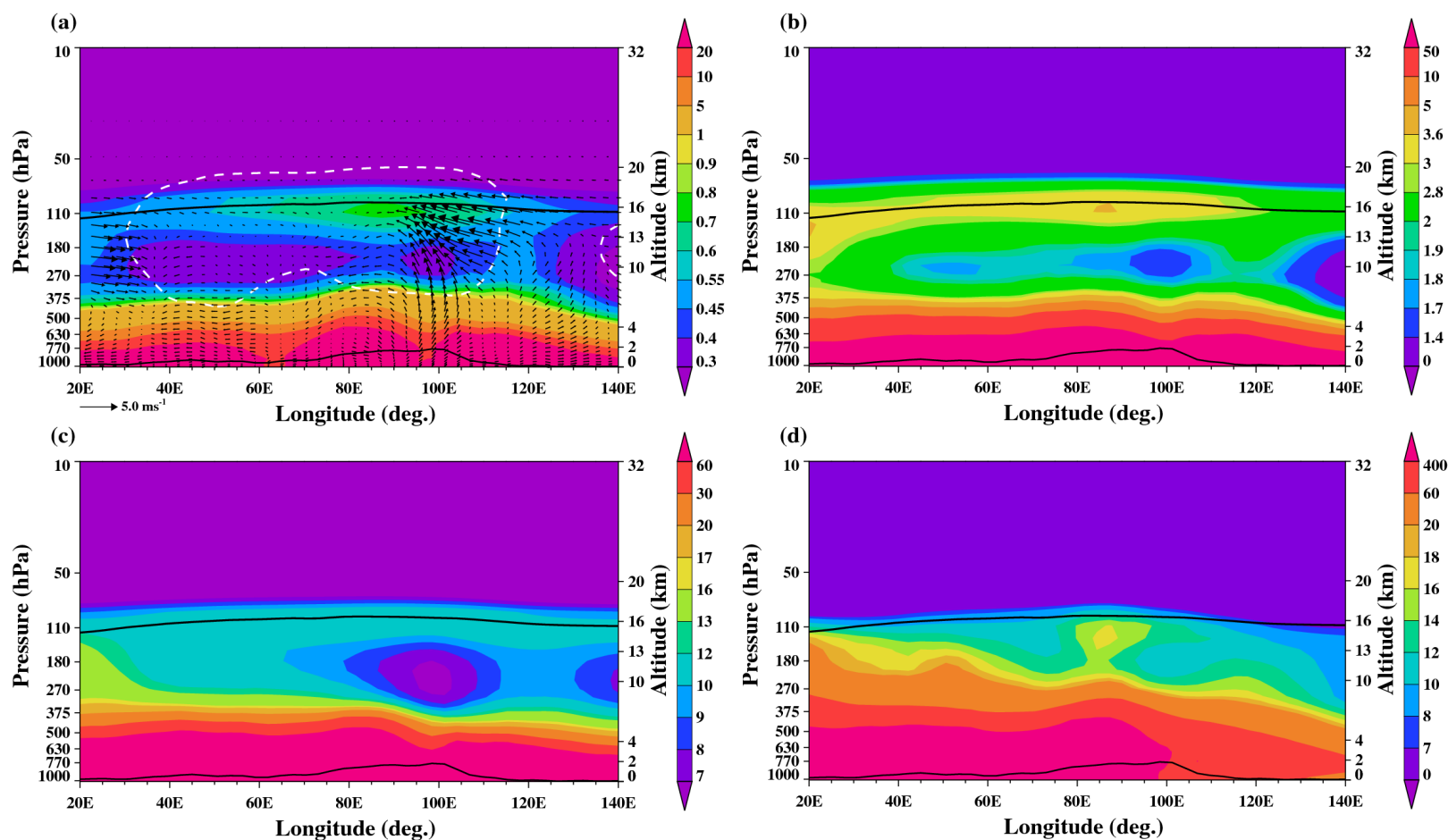


Figure 2. Longitude–pressure section (averaged for June–September and 15–35°N) of concentrations (ng/m³) of (a) BC aerosols, location of the monsoon anticyclone indicated with dotted line, (b) OC aerosols, (c) SO₄²⁻ and (d) Mineral dust aerosols. Vectors of the circulation are shown in (a) with the vertical wind scaled by 300. The upper black line marks the latitudinal averaged tropopause showing increased height in the ASM region. The lower black line marks the topography. The dashed white line is the negative 10⁻⁵ vorticity contour showing the approximate region of the anticyclone.

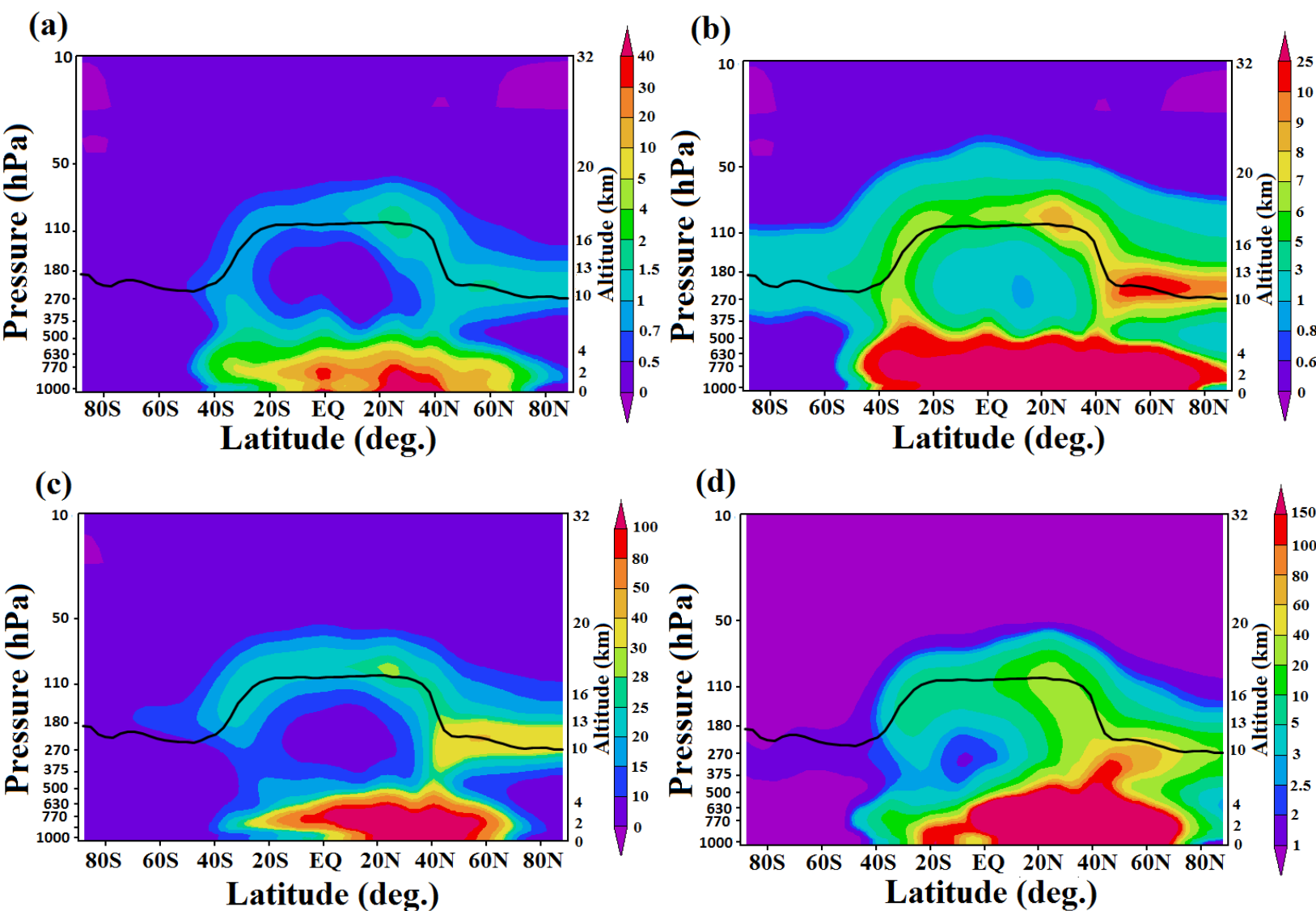


Figure 3. Latitude-pressure section (averaged for June-September and $60\text{-}120^{\circ}\text{E}$) of concentrations (ng/m^3) of (a) BC aerosols, location of the monsoon anticyclone indicated with dotted line, (b) OC aerosols, (c) SO_4^{2-} aerosols, (d) Mineral dust aerosols. The black line marks the longitudinally averaged tropopause showing increased height in the ASM region.

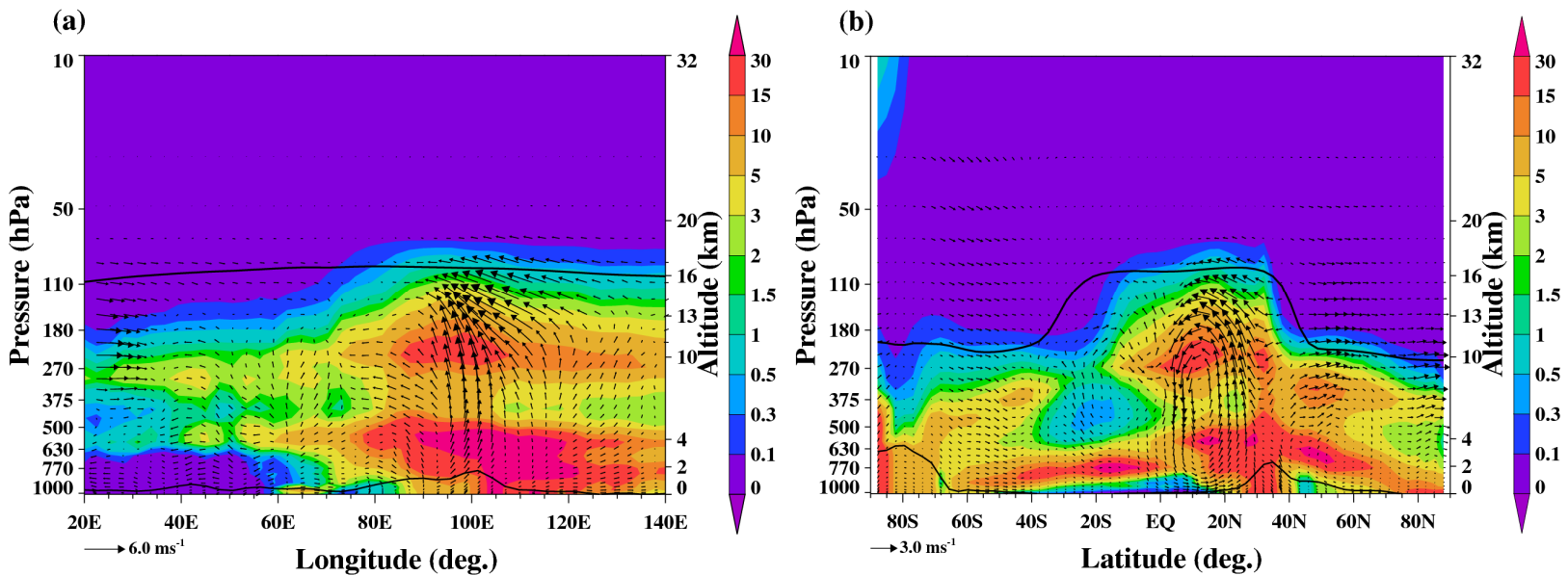


Figure 4. Distribution of Cloud Droplet Number Concentration (CDNC) and Ice Crystal Number Concentration (ICNC) (1/mg) averaged for June-September 2003. (a) Latitude average between 20°N and 30°N and (b) zonal average between 60°E and 120°E.

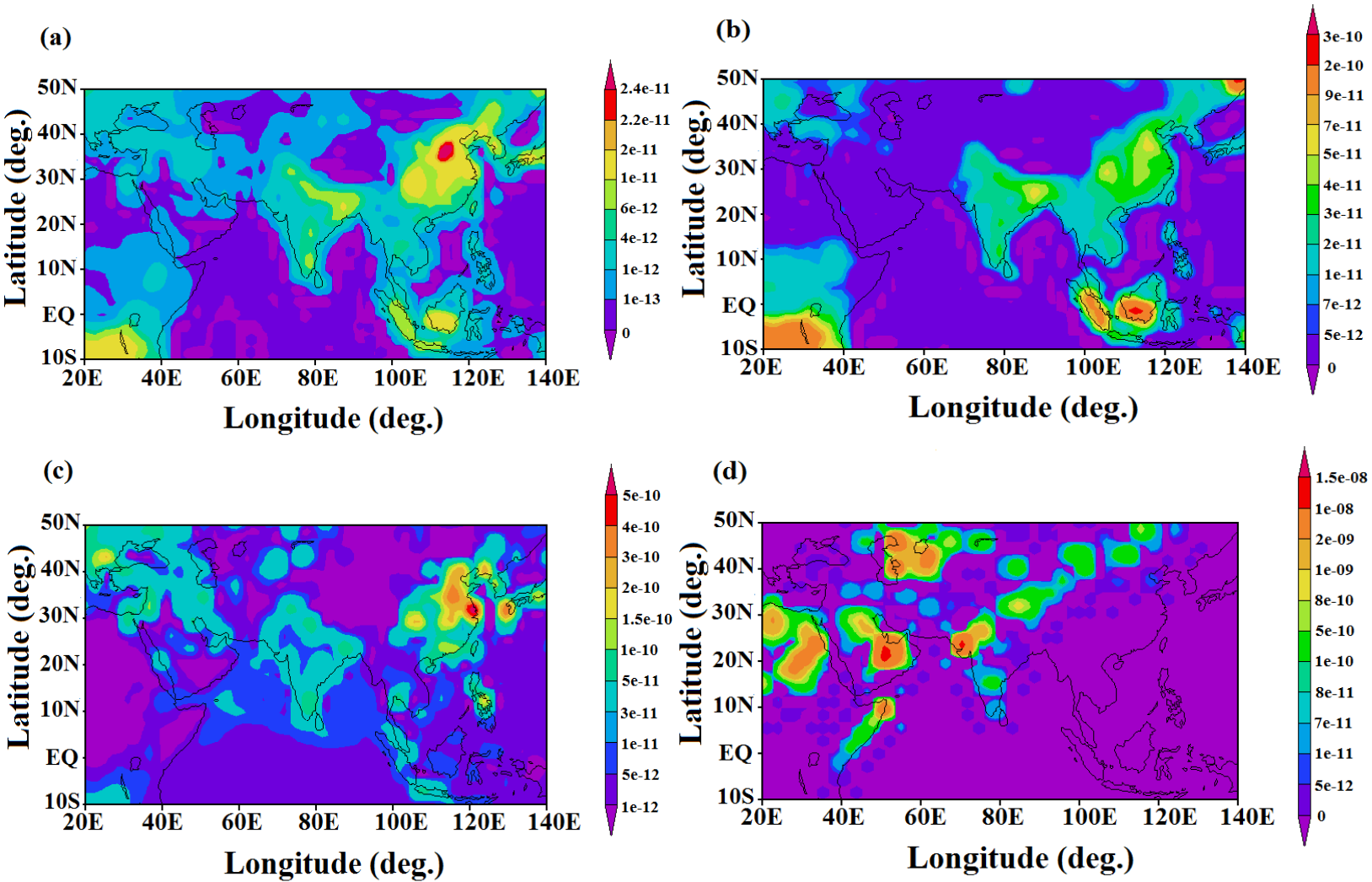


Figure 5. Distribution of emission mass flux (kg/m²/s) averaged for June-September 2003 for (a) BC, (b) OC, (c) SO₄²⁻ and (d) mineral dust.

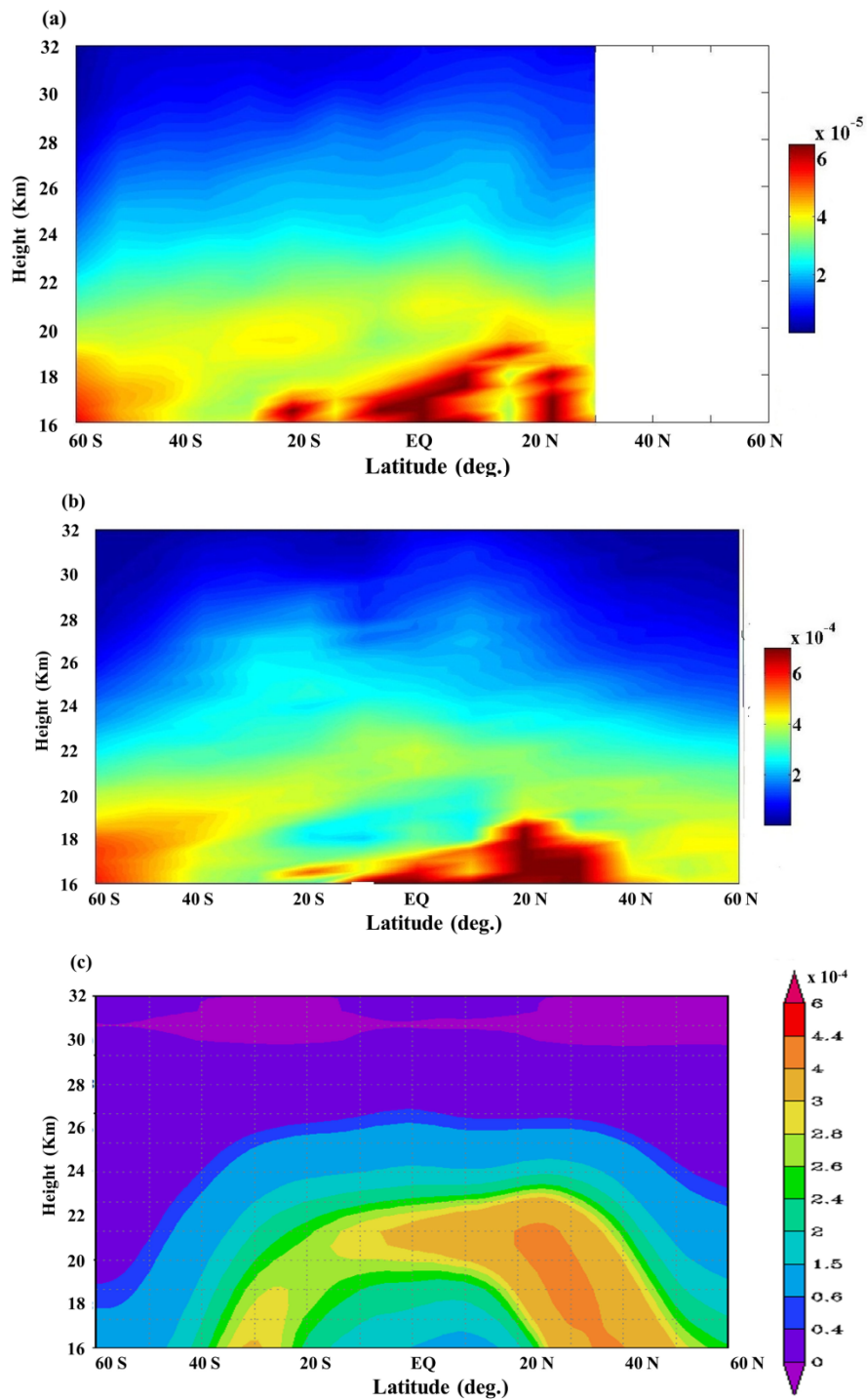


Figure 6. Latitude–pressure section (averaged for June–September and 60–120⁰E) of aerosol extinction (km^{-1}) as obtained from (a) HALOE 5.26 μm for the year 2003 (b) SAGE II 0.525 μm (c) ECHAM5-HAMMOZ simulations 0.550 μm for the year 2003 at the altitude 16–32km

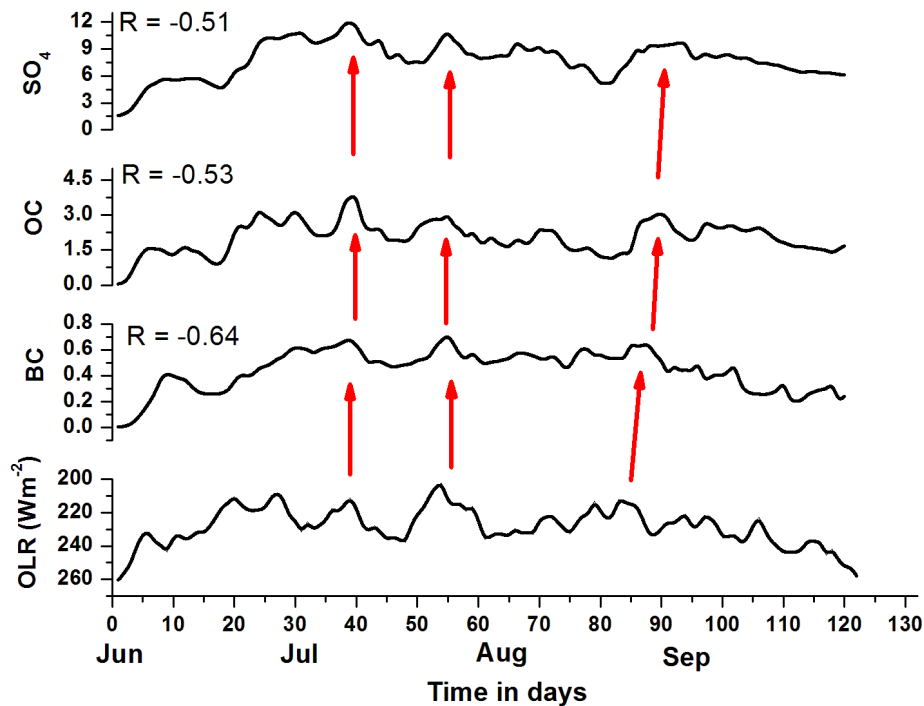


Figure 7. Time series of OLR (Wm^{-2}) averaged over ($15\text{-}30^\circ\text{N}$, $60\text{-}120^\circ\text{E}$) and ECHAM5-HAMMOZ simulated concentrations (ng/m^3) of BC, OC, SO_4^{2-} averaged over $20\text{-}30^\circ\text{N}$ and $60\text{-}120^\circ\text{E}$. Note that the scale for OLR is inverted. The anti-correlation coefficient of BC, OC, SO_4^{2-} with OLR is indicated at the top of the each panel.

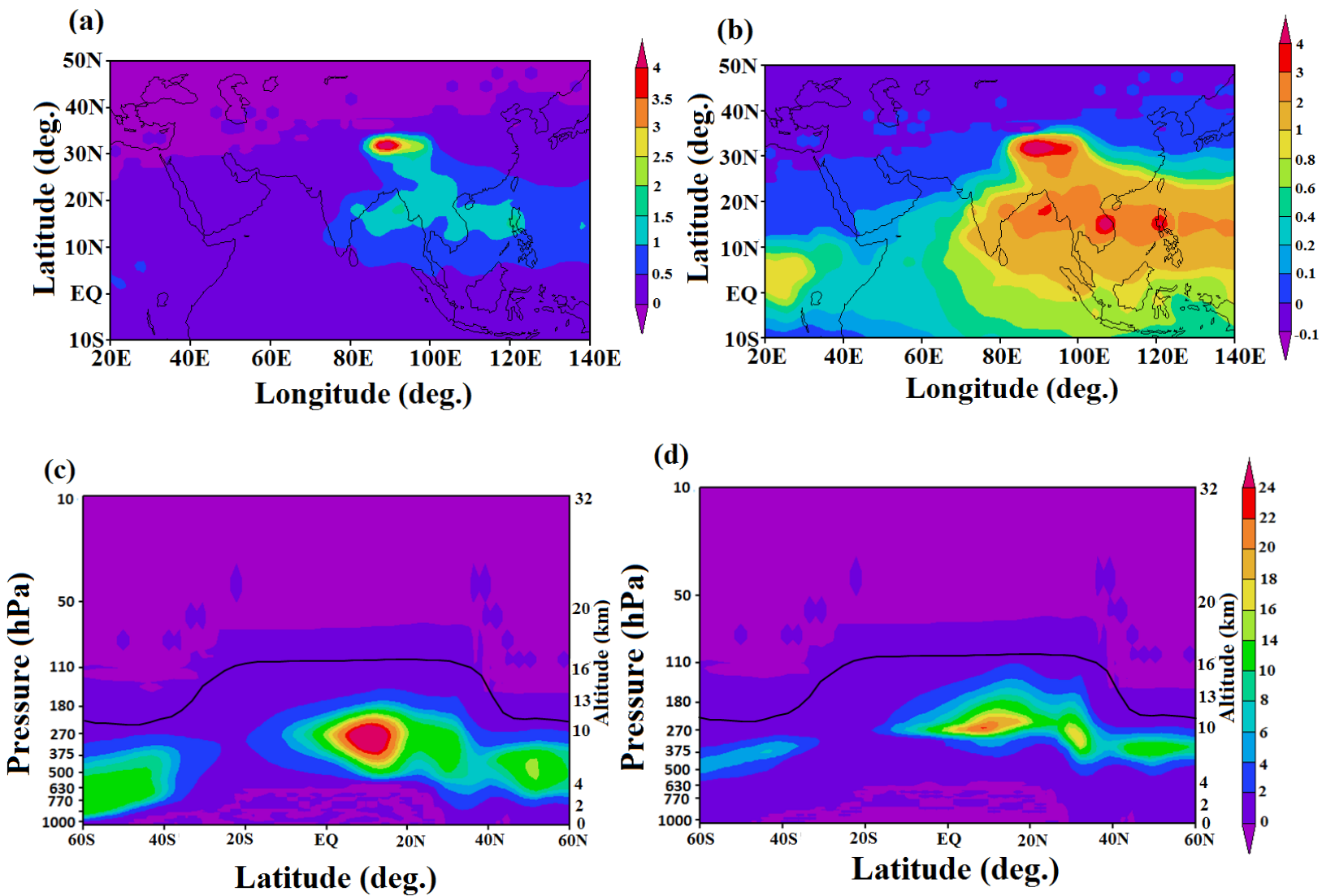


Figure 8. (a) Horizontal structure as obtained from ECHAM5-HAMMOZ CTRL simulations (averaged for ASM) of (a) cloud ice water (decigram/m^2) at 110 hPa, (b) ice crystal number concentration ($1/\text{mg}$) at 110 hPa, (c) Latitude-pressure cross section (averaged for June-September and $60\text{-}120^\circ\text{E}$) of cloud ice water (decigram/m^2), (d) Latitude-pressure cross section (averaged for June-September and $60\text{-}120^\circ\text{E}$) of ice crystal number concentration (ICNC) ($1/\text{mg}$).

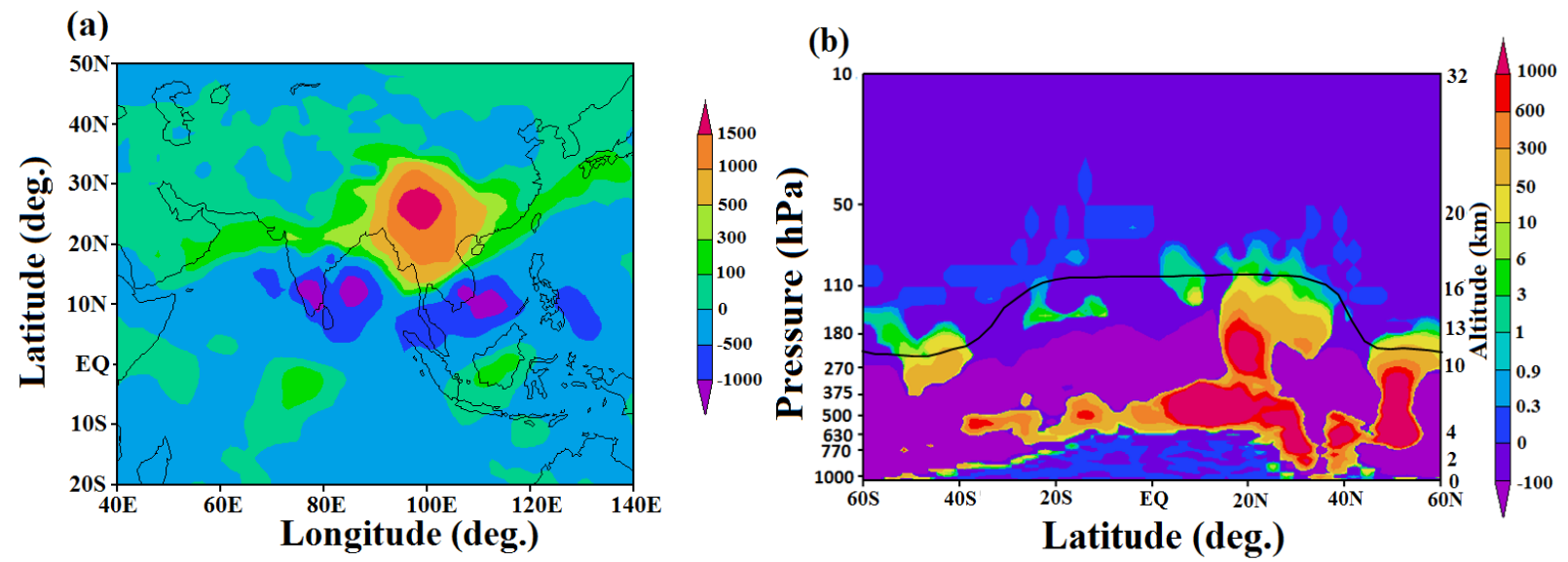


Figure 9. Spatial structure of mean cloud ice ($\mu\text{g}/\text{m}^3$) anomalies as obtained from ECHAM5-HAMMOZ CTRL - NOAER runs during ASM. (a) Pressure level slice at 181 hPa. (b) Latitude-pressure distribution averaged over 60-120°E.

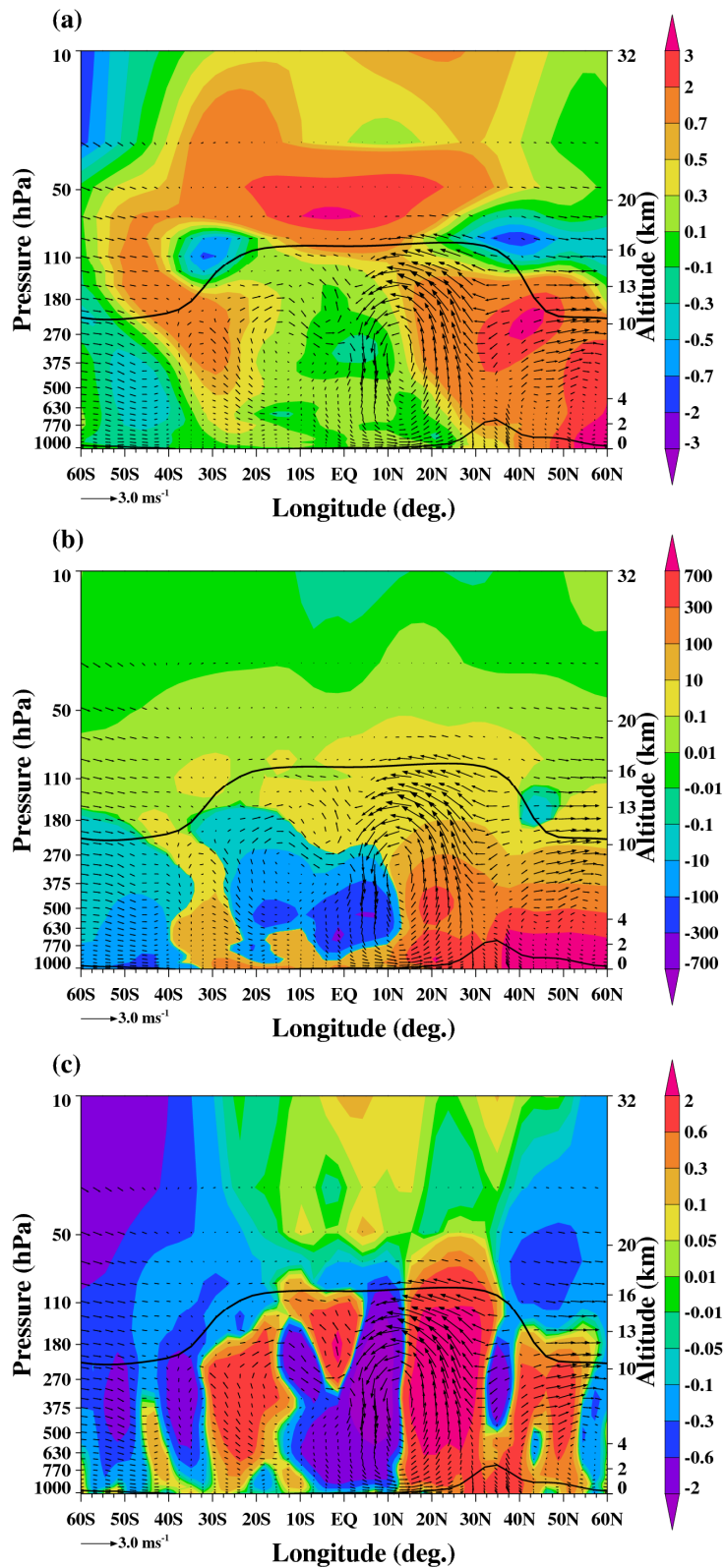


Figure 10. Latitude-pressure structure (averaged over 60-120°E) of difference between ECHAM5-HAMMOZ CTRL - NOAER runs during ASM for (a) temperature (K), (b) water vapor (ppmv) and (c) vertical wind (mm/s, not scaled). The meridional circulation is shown as a vector field (the vertical velocity field has been scaled by 300 and the units are m/s).

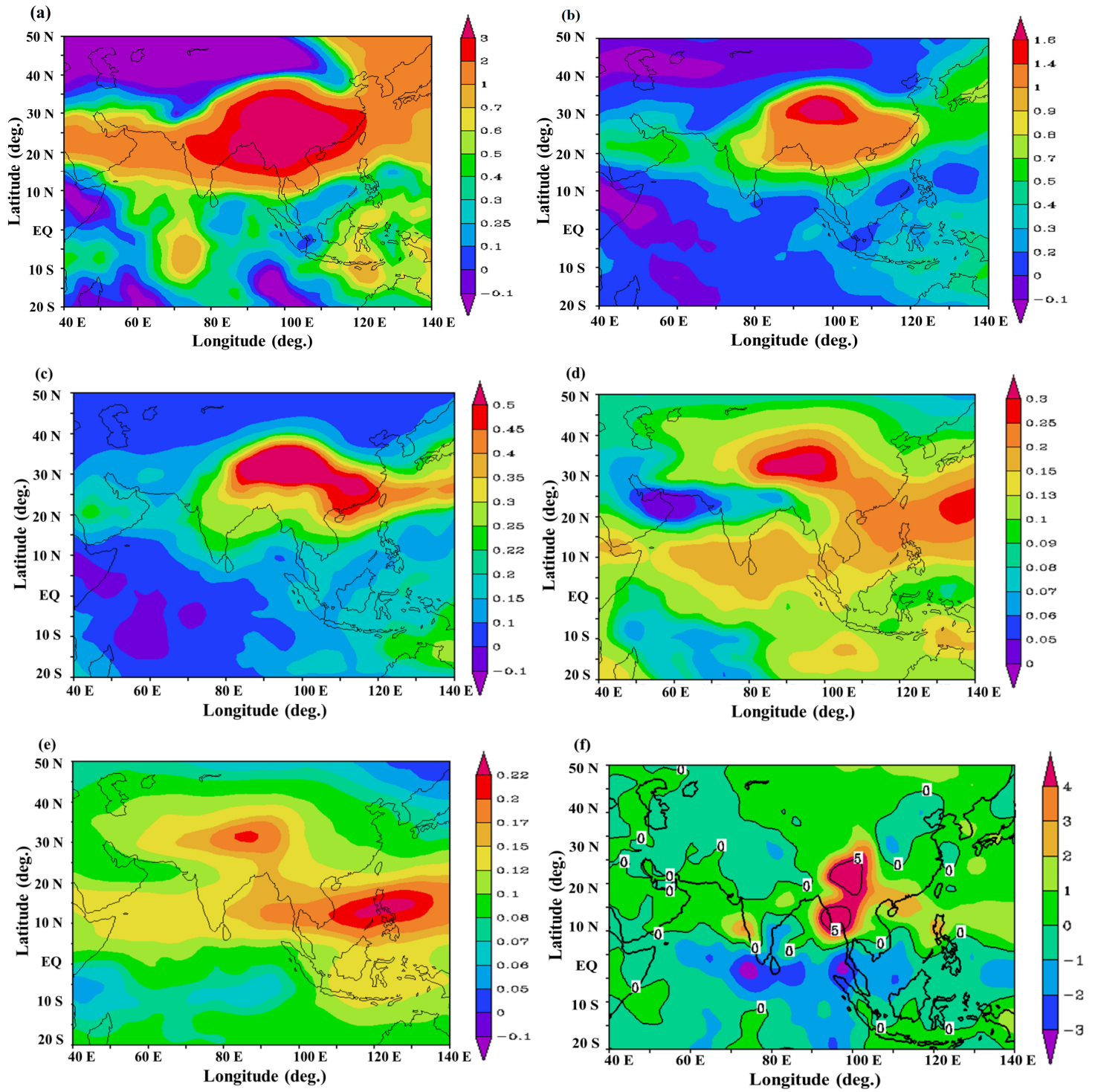


Figure 11. (a) Spatial structure of mean water vapor (ppmv) anomalies obtained from ECHAM5-HAMMOZ CTRL NOAER runs during ASM at (a) 155 hPa, (b) 132 hPa, (c) 110 hPa, (d) 90 hPa, (e) 70 hPa and (f) Spatial distribution of mean (JJAS) precipitation (mm/day) anomalies.